Matter

CellPress
OPEN ACCESS

Article

Absorbing stress via molecular crumple zones: Strain engineering flexibility into the rigid UiO-66 material

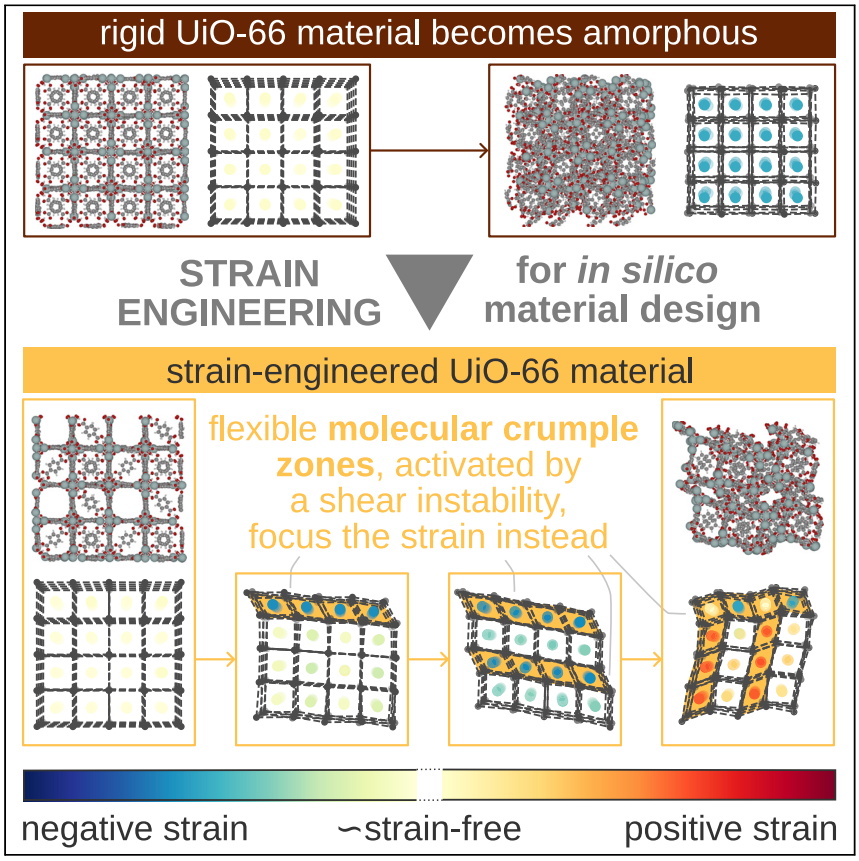

We introduce strain engineering as a computational approach to draw relationships between a material's atomic structure and its macroscopic behavior. We firstly strain engineer locally flexible crumple zones in a rigid material. Like vehicular crumple zones, they focus the strain when the material deforms and essentially preserve its rigidity and porosity. Secondly, strain engineering unveils the origins behind phase coexistence in flexible metal-organic frameworks. Given its general applicability, we anticipate that strain engineering will aid the design of state-of-the-art functional materials.

3 **Understanding**
Dependency and conditional studies on material behavior

Sven M.J. Rogge, Sander Borgmans, Veronique Van Speybroeck

sven.rogge@ugent.be

Highlights

Strain engineering as a design tool to correlate material structure and mechanics

4D strain fields form a material-transcending and experimentally measurable metric

Strain-engineered crumple zones focus strain and preserve the material's integrity

Prediction of a mechanical analogue of Braess's paradox in strain-engineered UiO-66

Rogge et al., Matter 6, 1435–1462
May 3, 2023
https://doi.org/10.1016/j.matt.2023.02.009

Matter

CellPress
OPEN ACCESS

Article

Absorbing stress via molecular crumple zones: Strain engineering flexibility into the rigid UiO-66 material

Sven M.J. Rogge,[1,2,3,*] Sander Borgmans,[1] and Veronique Van Speybroeck[1]

SUMMARY

Nanostructured materials such as metal-organic frameworks and perovskites can be tuned toward applications ranging from sensors to photovoltaic devices. Such design requires causal relations between a material's atomic structure and macroscopic function, which remain elusive. Therefore, we herein introduce strain engineering as a general approach to rationalizing and designing how atomic-level structural modifications induce dynamically interacting strain fields that dictate a material's macroscopic mechanical behavior. We first demonstrate the potential of strain engineering by designing shear instabilities in UiO-66, leading to counterintuitive behavior. The strain-engineered structures exhibit time- and space-dependent crumple zones that instill flexibility in the rigid material and locally focus the strain, partially preserving the material's porosity under compression. Secondly, our strain fields help explain stimulus-induced phase coexistence in the flexible CoBDP, DMOF-1(Zn), and MIL-53(Al)-F materials. These examples demonstrate how strain engineering can be adopted to design state-of-the-art materials for challenging applications from the atomic level onward.

INTRODUCTION

Metal-organic frameworks (MOFs), covalent organic frameworks (COFs), and perovskites are so-called nanostructured building block materials, as their overall structure can be decomposed into smaller, isolated building units. This makes these materials the ideal supramolecular platforms to design devices with exceptional properties—adsorption capacity, photovoltaic efficiency, separation performance, stability—by consciously fine-tuning their atomic structure while simultaneously retaining the overall connectivity of the material.[1–4] For instance, Krause et al. investigated how replacing the organic building block in the negative gas adsorption (NGA) DUT-49 material affects its adsorption behavior.[5] They found DUT-50, with an elongated linker compared with DUT-49, to exhibit both a higher pore volume and a larger pore size compared with the parent material while retaining the **fcu** topology and the adsorption-induced transition mechanism responsible for NGA in its parent material.[6] Similarly, (partially) exchanging the halide anion in cesium lead halide perovskites is an often-pursued approach to finely tune the optical properties and stability of these materials.[7,8] By replacing or even removing entire building blocks in this way, a combinatorially extensive versatility in hypothetical materials can be generated—each forms a potential contender for specific applications. Therefore, the key to sensibly exploring this vast design space and finding promising materials for specific applications is to establish causal relationships between the atomic structure of a material on the one hand and the resulting impact thereof on its

PROGRESS AND POTENTIAL

Controlling polymorphism in nanostructured materials such as metal-organic frameworks and perovskites is crucial to design, e.g., sensors or solar cells. Causal relationships between a material's atomic structure and macroscopic mechanical behavior are key to enabling such a design, yet they are still lacking. Here, we develop strain engineering as an *in silico* approach to draw such relationships. As an example, we strain engineer flexible crumple zones in the rigid UiO-66. Like crumple zones in cars, they locally focus the strain, thereby largely preserving the material's rigidity and porosity. We demonstrate the generalizability of our approach toward other materials and strain triggers by shedding light onto the origins of phase coexistence in soft porous crystals. As strain engineering is rooted in experimentally accessible strain fields that evolve through time and space, we anticipate that our technique will aid the design of state-of-the-art materials for challenging applications.

macroscopic behavior on the other. This goal immediately highlights a first crucial requirement when developing a material-transcending design tool: it should be able to accurately isolate and quantify the impact of atomic-level structural changes on a material's macroscopic behavior. In this work, we will demonstrate that strain engineering fulfills this requirement by drawing relationships between the atomic structure and the macroscopic mechanical behavior of any building block material, including MOFs, COFs, and perovskites.

The macroscopic behavior of MOFs and COFs is mediated by an interplay between stronger but local interactions, such as covalent and, for MOFs, coordination bonds, and weaker but much more spatially extended interactions, such as hydrogen bonds and van der Waals interactions.[9–12] This interplay makes these materials exhibit "anomalous" but desirable macroscopic responses to external stimuli (temperature, pressure, guest adsorption, etc.) that are not commonly found in more conventional materials.[13–16] Examples of these include negative linear compressibility,[17,18] auxeticity,[19] and NGA.[5,6] However, the presence of these long-range interactions also implies that minor alterations can impact the macroscopic behavior of the material far beyond where the alteration occurred. In addition, alterations at different locations in the material may interact and either strengthen or weaken one another, thereby leading to synergistic phenomena. For instance, locally adding organic struts in MOF-520 or NOTT-100 stabilizes the whole structure, leading to retrofitted analogs of these materials that can withstand much higher pressures than their parent material.[20,21] On a more extended scale, depositing metal halide perovskite thin films on a glass substrate and subsequently heating up or cooling down the composite introduces an interfacial strain that alters the phase stability and hence the photovoltaic properties of the entire material.[22] However, this long-range spatial extent over which alterations affect the material, and their often intricate interactions, complicate the disentanglement of any observed macroscopic effect into its different causal origins. This complexity is especially present when one has to account for confounding factors during the experimental measurement. As a result, predicting how different atomic-level alterations may interact with one another, even at long range, to synergistically impact a material's macroscopic behavior forms an important second challenge for any design tool.

As we will argue in this article, strain fields form a unique metric to establish a design tool that fully meets these two requirements. Strain fields are deformation fields that emerge whenever a material deviates from its equilibrium structure in response to strain sources. Such strain sources steer the material out of its defect-free equilibrium. They typically correspond to external stimuli or spatial disorder,[23–26] the latter of which can be either present intrinsically or introduced through defect engineering.[27,28] More specifically, consider a building block material that can be fully separated into non-overlapping parallelepipeds $\mathbf{h}_{\mu\nu\kappa}$. In this notation, the 3× 3 matrix $\mathbf{h}_{\mu\nu\kappa}$ contains the three vectors spanning this parallelepiped with indices (μ, ν, κ) (see experimental procedures for an illustration). This division into parallelepipeds is not unique. One can always merge adjacent parallelepipeds into larger ones, for instance to mimic the spatial resolution attainable by experimental strain characterization techniques.[29] The Lagrangian strain $\boldsymbol{\eta}_{\mu\nu\kappa}(t)$ experienced by the cell at an arbitrary location (μ, ν, κ) and at an arbitrary time t is then defined as

$$\boldsymbol{\eta}_{\mu\nu\kappa}(t) = \frac{1}{2}\left[\mathbf{h}_{\mathrm{ref},\mu\nu\kappa}^{-T}\mathbf{h}_{\mu\nu\kappa}^{T}(t)\mathbf{h}_{\mu\nu\kappa}(t)\mathbf{h}_{\mathrm{ref},\mu\nu\kappa}^{-1} - \mathbf{1}\right]. \qquad \text{(Equation 1)}$$

In this expression, $\mathbf{h}_{\mathrm{ref},\mu\nu\kappa}$ is an appropriately chosen, time-independent reference parallelepiped, $\mathbf{1}$ is the unit tensor, $\mathbf{a}^{-1}$ and $\mathbf{a}^{T}$ are the inverse and the transpose

[1]Center for Molecular Modeling (CMM), Ghent University, Technologiepark-Zwijnaarde 46, 9052 Zwijnaarde, Belgium

[2]Twitter: @sven_rogge

[3]Lead contact

*Correspondence: sven.rogge@ugent.be

https://doi.org/10.1016/j.matt.2023.02.009

of the matrix $\mathbf{a}$, and $\mathbf{a}^{-T} = (\mathbf{a}^{-1})^T$. By construction, these 3×3 Lagrangian strain tensors capture the evolution of the cell through both time and space. As this dimensionless strain metric, which reduces to the zero tensor in equilibrium, can be calculated over all cells constituting the material, this procedure gives rise to a spatially varying tensor field extending over the whole material. Moreover, it allows one to follow the propagation of the strain through the material over time.

Strain fields have not yet been examined for the nanostructured materials of interest here. However, various examples in less complex nano- and microstructured metals demonstrate that they can successfully isolate and differentiate between different strain sources,[25,30–34] thereby meeting the first requirement stated above. Furthermore, strain fields extend over length scales beyond the disorder they originate from, from a few unit cells up to the crystal size. As they can describe how different strain sources interact and cooperatively strengthen or weaken the material,[25,35] they also cover the second requirement. Additionally, experimental techniques such as transmission electron microscopy (TEM), X-ray diffraction (XRD), and grazing incidence wide angle X-ray scattering (GIWAXS) have recently matured to a level that they can manipulate and measure strain fields in nanostructured materials at or near atomic resolution.[36–43] This enables a thorough validation of this *in silico* design approach.

Building on these promising perspectives, we will herein introduce strain engineering as a design tool for functional nanostructured materials. More specifically, we aim to expand the thermodynamic conditions under which UiO-66, one of the most studied MOFs to date, remains stable.[44] UiO-66 is the ideal test system to demonstrate the potential of strain engineering, given its high tunability through postsynthetic modifications,[45–50] due to its relatively high thermal,[51,52] mechanical,[53–56] and chemical stability.[51,57,58] In its ideal, defect-free form, UiO-66(Zr) consists of inorganic $[Zr_6(\mu_3\text{-}O)_4(\mu_3\text{-}OH)_4]^{12+}$ building blocks that are 12-fold coordinated by organic benzenedicarboxylate linkers.[44] However, in reality, UiO-66 materials exhibit structural defects such as linker or inorganic node vacancies, which lower the coordination number of the (remaining) inorganic bricks.[27,51,59–64] Importantly, these defects are observed to interact with one another cooperatively. For instance, the relative orientation of adjacent linker vacancies dictates the mechanical stability of the resulting material.[56] In addition, linker vacancies preferentially conglomerate into defective nanodomains when present in large concentrations.[37,64] Defects are known to deteriorate the stability of the material,[56,65,66] for instance by decreasing the critical pressure above which the material becomes amorphous and irreversibly loses its structural integrity.[55,56,65] However, they can also increase the material's porosity and create preferential adsorption sites not present in the defect-free material.[28]

At this point, the question arises as to whether defects can be consciously designed in UiO-66 in such a way that they cooperatively interact in order to expand the volume range over which the material remains porous and stable while simultaneously limiting the decrease in the critical pressure that the material can withstand before irreversibly losing its structural integrity. Herein, we demonstrate that strain engineering is a valuable tool in this respect, as it rationalizes how shear instabilities form sacrificial crumple zones in UiO-66 that locally focus the strain—very similar to the effect of such crumple zones in vehicles. These local zones of flexibility preserve the structural integrity and, to a large extent, the material's porosity over a substantially larger range of volumes than the defect-free parent material. Subsequently, we take this strain engineering concept a step further by introducing two

orthogonal directions along which the material is prone to shear instability. We demonstrate that this results in cooperative effects where the intersections of two orthogonal crumple zones show a lower strain and a higher porosity than expected from two isolated and non-interacting crumple zones, an effect that can be fully understood through the strain engineering concept. Finally, we generalize our approach by providing new insight into how different thermodynamic triggers—pressure, temperature, gas adsorption—affect phase coexistence in pillared-layered soft porous crystals. We predicted earlier that this phenomenon could be accessed via specific experimental pathways, although the actual experimental realization of phase coexistence in these materials is still pending.[67] Our strain engineering analysis not only provides insight into the factors driving phase coexistence; the resulting strain fields also form experimentally accessible fingerprints that characterize phase coexistence in these soft porous crystals. This generalization, in terms of both materials and strain triggers, demonstrates the broad applicability of strain engineering to design novel materials.

RESULTS

UiO-66 materials selection to introduce the strain engineering concept

Defect-free UiO-66, shown schematically in Figure 1A, is a highly connected and rigid framework material. Each of the four inorganic building blocks in its unit cell, indicated by the white spheres, contains six 8-fold coordinated zirconium cations and is itself coordinated by 12 benzene-1,4-dicarboxylate (BDC) ligands. By removing, from the 24 organic linkers present in the unit cell, two parallel but non-collinear linkers, the material can be made susceptible to a shear deformation, as indicated with the orange arrow in Figure 1C. Removing only two linkers thus introduces a potential crumple zone where the material can locally absorb stress while maximally preserving the connectivity of the defect-free UiO-66 material. As a result of this procedure, all inorganic nodes in the unit cell have a reduced coordination number of 11, consisting of inorganic bricks in which two out of six zirconium cations are 7-fold instead of 8-fold coordinated. In Rogge et al.,[56] this specific structure was introduced as the **defect 5** structure. The same procedure can be repeated to remove an additional set of two parallel but non-collinear linkers that make a 90° angle with the original two linker vacancies. In this way, a second direction along which the material is prone to a shear instability is created, as visualized in Figure 1E. This procedure further reduces the coordination number of each inorganic node to ten.

Besides these three main structures of interest—the defect-free UiO-66 material and the two defective materials with either one or two orthogonal directions of shear instability—three intermediate defective structures have been constructed. The material of Figure 1B is obtained by removing one linker from the defect-free material, hence interpolating between the structures of Figures 1A and 1C. It corresponds to the **defect 0** structure of Rogge et al.[56] Likewise, the two materials in Figure 1D interpolate between the structures of Figures 1C and 1E, containing three linker vacancies per unit cell.

For each of these six materials, the temporal and spatial evolution of the strain induced in the structure through compression will be determined. To allow for sufficient spatial variation, each unit cell will be divided into 2×2×2 parallelepipeds following the procedure outlined in the experimental procedures. Each such parallelepiped fully contains one tetrahedral UiO-66 pore. In addition, a system consisting of 2×2×2 conventional unit cells will be simulated, resulting in a 4× 4× 4 grid

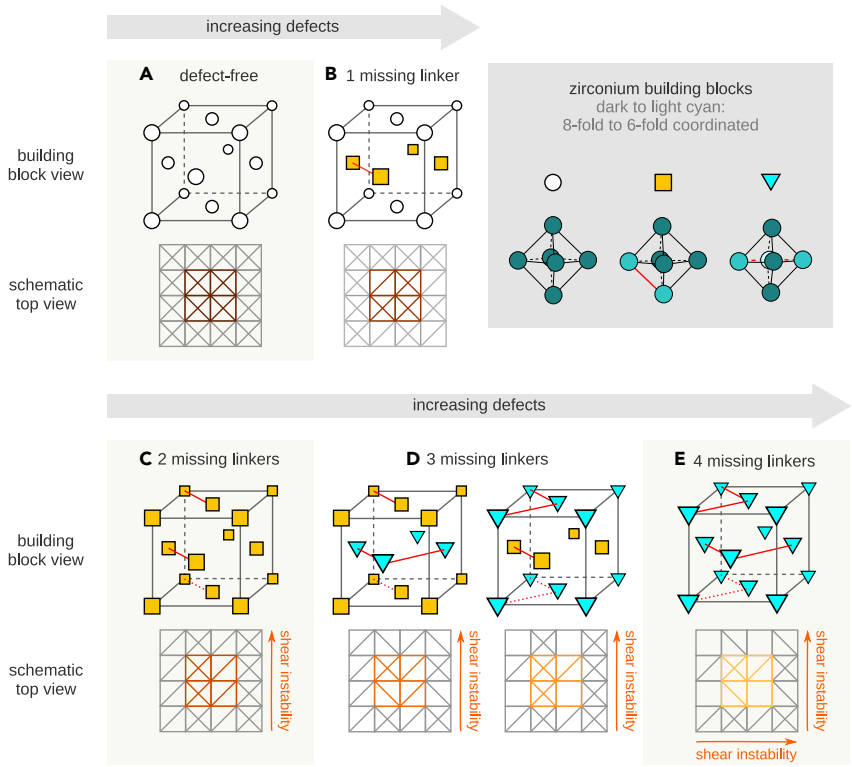

Figure 1. Selection of the defect-free and the five strain-engineered UiO-66 type materials

(A–E) Each material is composed of zirconium building blocks (represented by circles, squares, or triangles and whose coordination is given in the legend), which differ in the number of organic linkers they are bound to. Red lines in the building block view of the conventional unit cell represent linkers absent from the structure, which is also evident from the schematic top view of the remaining linkers in the simulated 2×2×2 supercells of the materials. Starting from the defect-free framework in (A), organic linkers are removed from the materials in (C) and (E). This is done in such a way that these strain-engineered materials become susceptible to either a single shear instability (first and third columns in the schematic of C) or two orthogonal directions of shear instability (first and third columns as well as first and third rows in the schematic of E). The materials in (B) and (D) are obtained by interpolating between the other three materials. As a result, the materials in (D) are also prone to shear instability along a single direction. Figure adapted from Rogge et al.[56] with permission from the American Chemical Society.

along which the strain field is quantified. The interactions between the different atoms will be modeled via system-specific force fields fitted to *ab initio* data obtained on the different building blocks of the six materials. As explained in detail in the experimental procedures, this building block approach increases the computational efficiency and maximizes the transferability of the interatomic potentials between the materials considered here.

The defect-free UiO-66 material as the reference to visualize strain fields

To set the scene, we start by determining how compression induces strain in the defect-free UiO-66 material. Starting from the strain-free equilibrium structure near a unit cell volume of 9,275 Å^3, Figure 2A shows that an isotropic negative strain develops through the material upon compression, which becomes more prominent the more significant the compression, from snapshot i to snapshot iv (see also Videos S1, S2, S3, and S4). A similar picture is obtained for each of the different uniaxial strain components η_{xx}, η_{yy}, and η_{zz}, resulting from the equivalence of these three

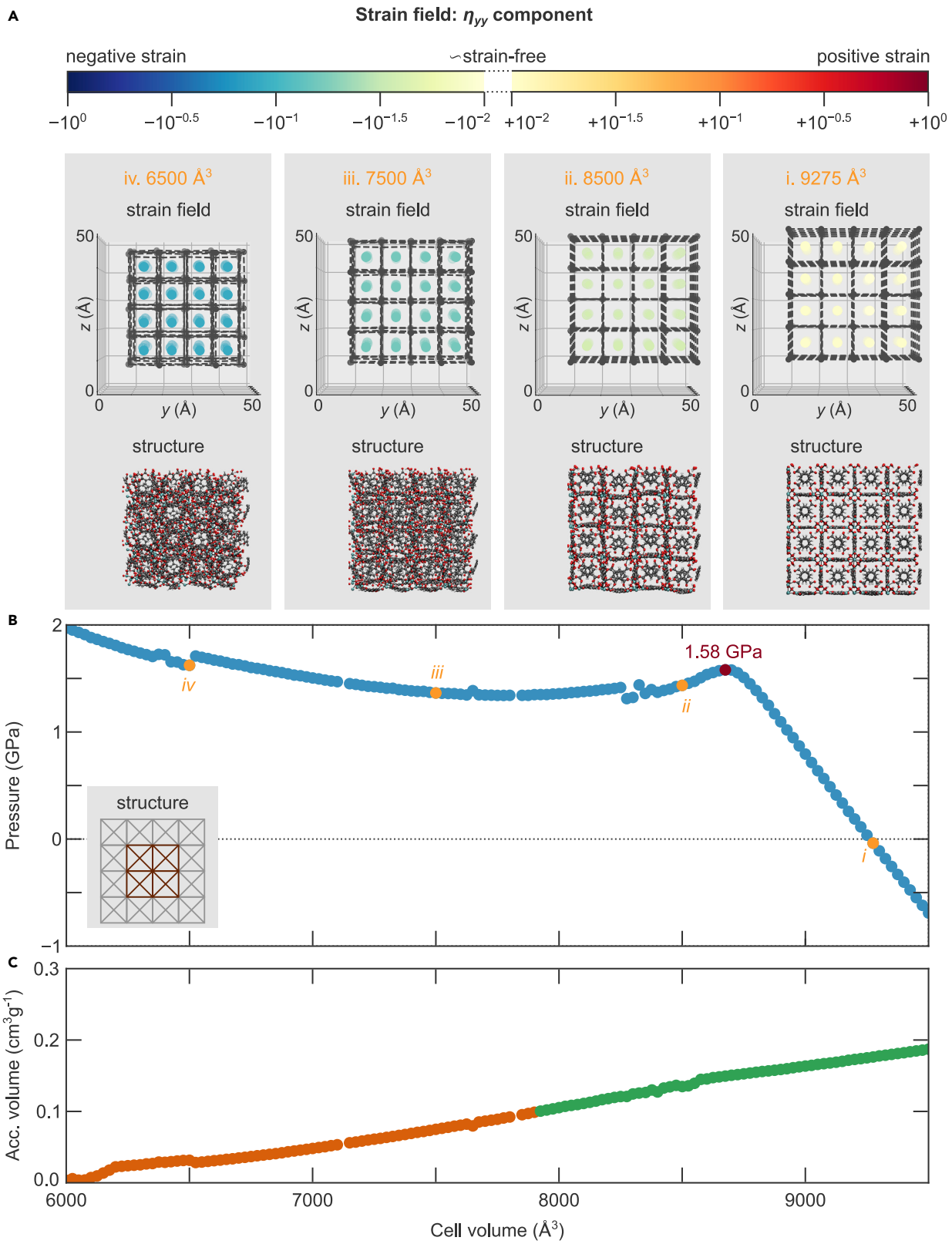
A
Strain field: η_{yy} component
negative strain
strain-free
positive strain
-10^{0}
$-10^{-0.5}$
-10^{-1}
$-10^{-1.5}$
-10^{-2}
$+10^{-2}$
$+10^{-1.5}$
$+10^{-1}$
$+10^{-0.5}$
$+10^{0}$
iv. 6500 Å^3
iii. 7500 Å^3
ii. 8500 Å^3
i. 9275 Å^3
strain field
structure
z (Å)
y (Å)
0
50
B
Pressure (GPa)
1.58 GPa
iv
iii
ii
i
structure
C
Acc. volume (cm^{3}g^{-1})
Cell volume (Å^3)
6000
7000
8000
9000

Figure 2. Homogeneous strain fields introduced in the defect-free UiO-66 material upon compression

(A) Atomic structures and corresponding uniaxial (η_{yy}) strain fields at four different volumes. The strain present in each region is color coded from yellow (low strain) to either blue (large negative strain) or red (large positive strain).

(B) Pressure-versus-volume equation of state at 300 K, with the transition pressure (red point) and the four structures found in (A) (orange points, numbered i to iv) indicated.

(C) Gravimetric accessible volume for a spherical probe with radius 1.2 Å as a function of the volume, color coded based on a hard cutoff at 0.10 cm^3 g.

directions in the defect-free material. In contrast, while the shear strains η_{xy}, η_{yz}, and η_{xz} are also homogeneous, they remain small even at the largest compressions, thanks to the high and isotropic connectivity in the defect-free UiO-66 material.

In order to gain additional insight into the pressure needed to realize this compression, the pressure-versus-volume equation of the state of the material is visualized in Figure 2B. As discussed in more detail in the experimental procedures, this equation of state reveals for which volume range the material is (meta)stable, characterized by a negative $\partial P/\partial V$ slope, and for which volumes the material is mechanically unstable, characterized by a positive $\partial P/\partial V$ slope. Regions of (meta)stability and instability are separated by maxima and minima in the equation of state, which correspond to the critical pressures that need to be applied to induce a phase transition from one to another (meta)stable state in the material. For our defect-free UiO-66 structure, the maximum in the pressure-versus-volume equation of state in Figure 2B, indicated in red, reveals that the material remains stable upon compression until it reaches a volume of 8,675 $Å^3$, which is reached when applying a pressure of 1.58 GPa. This critical pressure is a bit lower than the loss-of-crystallinity pressure found in our earlier study due to the different force-field descriptions (see experimental procedures)[56] but coincides well with available experimental studies.[55,65] When exceeding this critical pressure, the material collapses, resulting in the homogeneous strain and loss of structural integrity observed in Figure 2A.

To understand the impact of this loss of structural integrity on the material's porosity, Figure 2C reports the porous volume accessible for a probe of radius 1.2 Å over the same volume range as the pressure-versus-volume equation of state. Starting from a gravimetric accessible volume of about 0.17 $cm^3\ g^{-1}$ near equilibrium, the material's porosity quickly deteriorates and falls below 0.10 $cm^3\ g^{-1}$ already at a volume of about 7,900 $Å^3$. This surprisingly fast reduction in porosity—which is also reflected using other measures such as the absolute accessible pore volume or the accessible pore volume fraction—is a direct consequence of the homogeneous collapse of the entire structure at these volumes. The atomic snapshots in Figure 2A indeed show clear disorder for the smallest structures, akin to the experimentally observed amorphization at these volumes.[55] It is important to stress that the force-field-based approach adopted here cannot describe the reactive events underlying amorphization. As a result, the atomic structures ii to iv in Figure 2A, which do not show any bond reorganization, only approximate those found experimentally. However, the loss of crystallinity observed in Figure 2B was proven earlier to form an accurate proxy to describe the experimentally observed amorphization.[56]

In conclusion, the strain fields in Figure 2 confirm the experimentally observed rigidity of the defect-free UiO-66 material, with an exceptionally high loss-of-crystallinity pressure and a homogeneous strain distribution. On the downside, this rigidity also results in a strong and homogeneous reduction in porosity upon compression, making the amorphous material less suited for any adsorption-based application. As discussed in Note S1.1 and visualized in Videos S14, S15, S16, and S17, a similar picture arises for the material of Figure 1B containing a single linker vacancy. While this

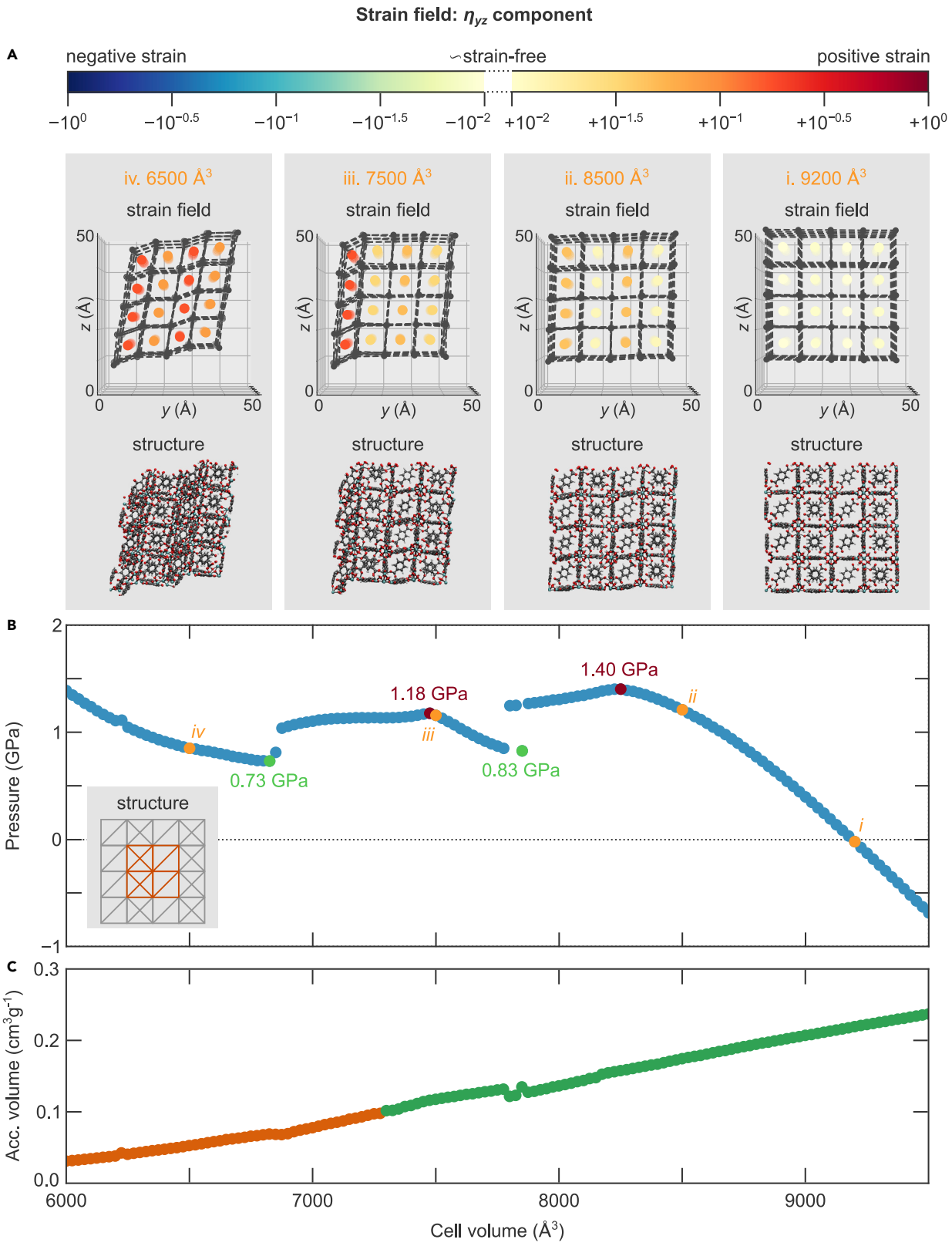
Strain field: η_{yz} component
A
negative strain
strain-free
positive strain
-10^{0}
$-10^{-0.5}$
-10^{-1}
$-10^{-1.5}$
-10^{-2}
$+10^{-2}$
$+10^{-1.5}$
$+10^{-1}$
$+10^{-0.5}$
$+10^{0}$
iv. 6500 Å^3
iii. 7500 Å^3
ii. 8500 Å^3
i. 9200 Å^3
strain field
structure
z (Å)
y (Å)
0
50
B
Pressure (GPa)
2
1
0
−1
1.40 GPa
1.18 GPa
0.73 GPa
0.83 GPa
iv
iii
ii
i
structure
C
Acc. volume (cm^{3}g^{-1})
0.3
0.2
0.1
0.0
6000
7000
8000
9000
Cell volume (Å^3)

Figure 3. Inhomogeneous strain fields showing the first shear instability introduced in the strain-engineered UiO-66 material containing two linker vacancies

(A) Atomic structures and corresponding shear (η_{yz}) strain fields at four different volumes demonstrate how the shear instability comes to expression in two steps (structures iii and iv). The strain present in each region is color coded from yellow (low strain) to either blue (large negative strain) or red (large positive strain).

(B) Pressure-versus-volume equation of state at 300 K, with the transition pressures (red and green points) and the four structures found in (A) (orange points, numbered i to iv) indicated.

(C) Gravimetric accessible volume for a spherical probe with radius 1.2 Å as a function of the volume, color coded based on a hard cutoff at 0.10 $cm^3\ g^{-1}$.

linker vacancy reduces the loss-of-crystallinity pressure of this material to about 1.47 GPa and increases its porosity near equilibrium to about 0.20 $cm^3\ g^{-1}$, it shows the same homogeneous distribution of the strain over the material and a similar reduction in porosity upon compression.

Strain engineering a first shear instability to create crumple zones

In a first attempt to expand the volume range for which the UiO-66 material is both stable and porous, we create a first shear instability by introducing two linker vacancies, as shown in Figure 1C. Our strain fields reveal that this profoundly affects the distribution of the strain throughout the material, as demonstrated in Figure 3A and Videos S5, S6, S7, and S8. In contrast to the strain fields of Figure 2A, we here focus on the shear strain components—more specifically, the η_{yz} strain—given the specific shear instability created in the material. Again, starting from a strain-free equilibrium structure around 9,200 $Å^3$, compressing the structure no longer leads to a homogeneous strain distribution. Instead, the strain is concentrated along the columns in the material that contain the linker vacancies. In those regions, the shear strain is about one order of magnitude larger than in the columns in which all linkers are present (panel ii in Figure 3A). Due to the counterclockwise shear instability, only positive shear strains are observed in this material.

This strain inhomogeneity intensifies when the material is further compressed, up to the point that the columns containing the linker vacancies move along the created shear instability (panels iii and iv in Figure 3A). In these columns, the strain is almost two orders of magnitude larger than in the other parts of the material, thereby acting as focus regions for the strain that relieve the remainder of the material. This stress relief occurs stepwise upon compression: the shear instability first comes to expression in a single column (panel iii), after which a second, parallel instability is induced for lower volumes (panel iv). Therefore, these two columns in the strain-engineered material act as so-called local crumple zones, which flexibly and reversibly transition from their equilibrium structure through a shear deformation to locally absorb the strain while retaining the structure of the other parts of the material.

The introduced crumple zone not only affects the strain distribution throughout the material but also profoundly changes its stability. In the pressure-versus-volume equation of state of Figure 3B, two additional metastable branches are introduced next to the stable branch near the equilibrium volume of 9,200 $Å^3$, which was also present in the defect-free material. These metastable branches are located between <6,000 $Å^3$ and 6,825 $Å^3$ and between 7,475 $Å^3$ and 7,850 $Å^3$. Inspecting the atomic structure at these volumes, visualized in Figure 3A, demonstrates that these branches correspond to volume regions in which one or two columns have transitioned along the shear instability. This occurrence of multiple metastable branches and the abrupt discontinuities between the different branches in the pressure-versus-volume equation of state are akin to the phase separation found earlier in soft porous crystals such as MIL-53(Al) and DMOF-1(Zn).[67] However, there is an important distinction: the defect-free UiO-66 material is a rigid MOF, in contrast

to the flexible MOFs for which phase coexistence was observed earlier. While these crumple zones also reduce the critical pressure the material can withstand from 1.58 GPa for the defect-free material to 1.40 GPa here, the strain-engineered material proposed here remains among the mechanically most stable MOFs. The presence of these crumple zones was overlooked in Rogge et al.,[56] as only volumes exceeding 8,000 $Å^3$ were investigated in that earlier study.

While the two additional mechanically stable branches indicate the possibility of stabilizing this strain-engineered material at these lower volumes, reaching these branches in an experimental setup is most likely not straightforward. This is because the two transition pressures encountered upon compression, 1.40 and 1.18 GPa, decrease upon decreasing volume. As a result, while applying a pressure above 1.40 GPa is necessary to activate a first crumple zone, maintaining this pressure would immediately induce a second crumple zone since it exceeds 1.18 GPa. One way to overcome this would be to pressure quench the material during the transition, as suggested in Rogge et al.[67] Alternatively, additional linker vacancies could be introduced in the material to further design these transition pressures such that they rather increase with decreasing volume (*vide infra*). The exact magnitude of the critical pressures and the number of metastable branches will be size dependent and, moreover, will be affected by the concentration of crumple zones in the material, similar to our earlier observation of layered phase coexistence in polymorphic MOFs and as investigated for the strain-engineered UiO-66 materials with three or four linker vacancies in Note S3.[67] However, given that we observed the same physical process through which the crumple zones are activated upon compression for all strain-engineered materials studied here, we expect this physical process to locally focus the strain, outlined above, to be size independent.

Finally, the strain-engineered material shows an increased porosity, even at lower volumes (Figure 3C). Given that the crumple zones focus the strain that is induced when compressing the material, the strain in the remainder of the strain-engineered material is substantially smaller than in the defect-free material at a similar degree of compression. As a result, the original porosity is retained locally in those relatively strain-free regions, and part of the material can still be used for adsorption-based applications.

Repeating this analysis for the materials in Figure 1D, both containing the same shear instability as the strain-engineered material discussed here, consistently shows the same picture, in which two additional mechanically stable branches emerge compared with the defect-free material thanks to the local flexibility in the structure (see Note S1.2 and Videos S18, S19, S20, S21, S22, S23, S24, and S25). However, given that a third linker vacancy is created in these materials, their critical pressures are lower than the ones here. Interestingly, for the material discussed in Figure S3, the transition pressures encountered under compression increase upon decreasing volume, constituting a first example where both crumple zones can be more easily accessed through a constant-pressure experiment. These examples demonstrate the need to judiciously balance how many and which linkers to remove when introducing crumple zones. Compared with Figure 3C, the more defective materials of Figure 1D show an even more pronounced porosity.

Strain engineering synergistically interacting crumple zones via a second, orthogonal shear instability

Guided by the encouraging observations when introducing a first crumple zone in the material, we here focus on the effect of introducing a second, orthogonal

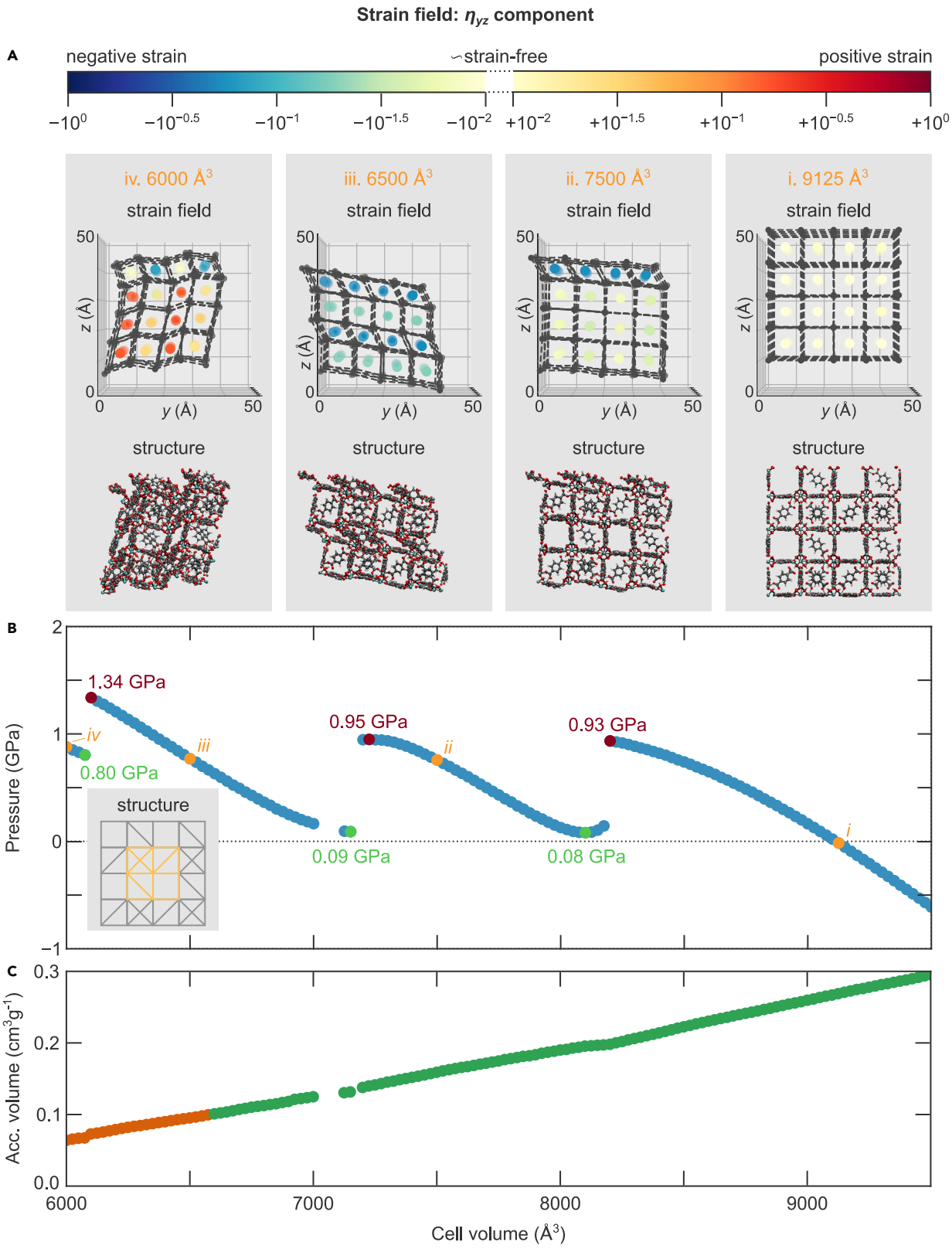
Strain field: η_{yz} component
A
negative strain
strain-free
positive strain
-10^{0}
$-10^{-0.5}$
-10^{-1}
$-10^{-1.5}$
-10^{-2}
$+10^{-2}$
$+10^{-1.5}$
$+10^{-1}$
$+10^{-0.5}$
$+10^{0}$
iv. 6000 Å^3
iii. 6500 Å^3
ii. 7500 Å^3
i. 9125 Å^3
strain field
structure
z (Å)
y (Å)
0
50
B
Pressure (GPa)
1.34 GPa
0.80 GPa
0.95 GPa
0.09 GPa
0.93 GPa
0.08 GPa
iv
iii
ii
i
structure
2
1
0
−1
C
Acc. volume (cm^{3}g^{-1})
0.3
0.2
0.1
0.0
6000
7000
8000
9000
Cell volume (Å^3)

Figure 4. Inhomogeneous strain fields showing the combination of two orthogonal shear instabilities introduced in the strain-engineered UiO-66 material containing four linker vacancies

(A) Atomic structures and corresponding shear (η_{yz}) strain fields at four different volumes demonstrate how the shear instability comes to expression in three steps (structures ii to iv). The strain present in each region is color coded from yellow (low strain) to either blue (large negative strain) or red (large positive strain).

(B) Pressure-versus-volume equation of state at 300 K, with the transition pressures (red and green points) and the four structures found in (A) (orange points, numbered i to iv) indicated.

(C) Gravimetric accessible volume for a spherical probe with radius 1.2 Å as a function of the volume, color coded based on a hard cutoff at 0.10 $cm^3\ g^{-1}$.

crumple zone, as shown in Figure 1E. Naively, without synergistic effects, we expect that due to this intervention, the pressure-versus-volume equation of state would reveal four metastable branches next to the stable branch also found for the defect-free material. The strain would then be concentrated along one or both of these orthogonal crumple zones. This latter effect would increase the sacrificial volume of the material—which porosity is lost when the crumple zone is active—from 50%, as in Figures 3, to 75% here. Figure 4 reveals that this strain-engineered material does show the expected metastable branches. However, instead of the expected 75%, only about 50% of the material's volume is sacrificial, similar to the value obtained for the material with only a single crumple zone. This is thanks to the interaction between the strain fields induced by the two orthogonal crumple zones.

When starting from the reference structure of the strain-engineered material around 9,125 $Å^3$ (panel i in Figure 4A; Video S9) and following the strain field during compression, reducing the volume introduces a first (panel ii in Figure 4A; Video S10) and then a second parallel (panel iii in Figure 4A; Video S11) crumple zone, eventually affecting 50% of the material. At this point, the observations are entirely in line with our expectations. However, when reducing the material's volume even further to induce a third, orthogonal crumple zone, the strain at those cells where the crumple zones intersect is partially annihilated (panel iv in Figure 4A; Video S12). This strain reduction stems from the additivity of the strain fields originating from the different crumple zones and the opposite signs of the introduced strain fields. As a result, the shear strain in the material is almost completely absent at those points of intersection, similar to the situation near the equilibrium structure despite the ca. 30% overall volume reduction of the structure.

The pressure-versus-volume equation of state (Figure 4B) shows three out of four expected mechanically stable branches next to the stable branch near the equilibrium volume, for which panels ii, iii, and iv are representative structures and strain fields. A fourth additional metastable branch is expected to occur at even lower volumes. However, the non-smooth character of the equation of state when going to a volume below 6,000 $Å^3$ indicates that our force-field description breaks down at that point. In contrast to Figure 3B, the transition pressures encountered in Figure 4B increase when decreasing the volume, from 0.93 GPa to over 0.95–1.34 GPa. This also implies that each branch can be accessed rather straightforwardly by applying a constant pressure. For instance, the mechanically stable branch between 6,100 $Å^3$ and 7,150 $Å^3$ can be reached by applying a pressure between 0.95 GPa and 1.34 GPa to the equilibrium structure. In comparison, the branch between 7,225 $Å^3$ and 8,100 $Å^3$ would require a narrow pressure window between 0.93 GPa and 0.95 GPa.

Besides fundamentally altering the flexible behavior of the material, the additional linker vacancy creation in this strain-engineered material drastically increases its porosity up to the point that the material retains a gravimetric accessible pore volume of 0.10 $cm^3\ g^{-1}$ down to volumes as low as 6,600 $Å^3$, as shown in Figure 4. In combination with the extended stability of the material, this opens the range of

conditions under which the material can be potentially adopted, conditional on the availability of appropriate experimental synthesis tools to target the creation of these specific types of linker vacancies.

The temporal evolution of orthogonally induced strain fields

Up to this point, we focused on the spatial variation of the strain fields and approaches on how to alter this variation via the conscious introduction of interacting crumple zones. Each of the strain fields in Figures 2, 3, and 4 are obtained by taking a time average of the strain field evolutions in the supplemental videos to obtain this equilibrium picture (Videos S1–S12). However, also the temporal evolution of these strain fields yields interesting information. In Figure 5, we highlight the temporal evolution of a strain field during the first 5.5 ps of a simulation when starting from the equilibrium structure of Figure 1E and applying a temperature of 300 K and a pressure of 1 GPa (a longer strain field evolution of this material is shown in Video S13). As anticipated in the section "Strain engineering synergistically interacting crumple zones via a second, orthogonal shear instability," Figure 4B predicts that a pressure of 1 GPa should result in two parallel crumple zones over time if the material remains in close thermodynamic equilibrium with its environment.

The time-dependent strain fields of Figure 5 show that the material starts to compress rapidly after applying a constant pressure of 1 GPa. As expected, the resulting strain is concentrated in the material's four crumple zones: the two horizontal crumple zones with a negative strain, and the two vertical crumple zones with a positive η_{yz} strain. This indicates that the reorganization of the strain over the whole material and its concentration into the crumple zones occur rather quickly. As such a rapid transition would be challenging to capture with experimental techniques given their temporal resolution, our *in silico* strain engineering approach provides unique and complementary insight into the spatiotemporal evolution of the phase transition.[29] Initially, the four crumple zones in Figure 5 become active simultaneously, given that the material is not in thermodynamic equilibrium during its transition and given the equivalence of these four crumple zones. After only about 3 ps, the strain in one of the horizontal crumple zones is released again and gets focused into one of the remaining three zones instead, a process finalized after about 5 ps. Afterward, the material remains in this configuration, similar to the equilibrated structure in panel iv of Figure 4A.

Compared with the equilibrium prediction in Figure 4B, a pressure of 1 GPa should steer the material to a configuration in which only two, not three, crumple zones are active, as in panel iii of Figure 4A. Figure 5 highlights the non-equilibrium character of the transition at constant pressure, which is not unexpected given the significant decrease in volume and the resulting work exerted on the material in the process. However, Figure 5 does predict that these crumple zones can also be activated through a non-equilibrium regular pressurization of the material. This paves the way to experimentally confirm the increased porosity and stability of these strain-engineered materials under a larger volume range, using the techniques outlined in the introduction, and to use these materials for pressure-induced shock absorption applications.

The potential of strain engineering for functional material discovery

At the onset of this work, we expressed our aim to establish strain engineering as a new design tool to consciously construct materials with exciting mechanical properties either from an application-oriented or a fundamental point of view. If successful, strain engineering would have the potential to substantially expand the functional material space either by altering and fine-tuning the thermodynamic conditions

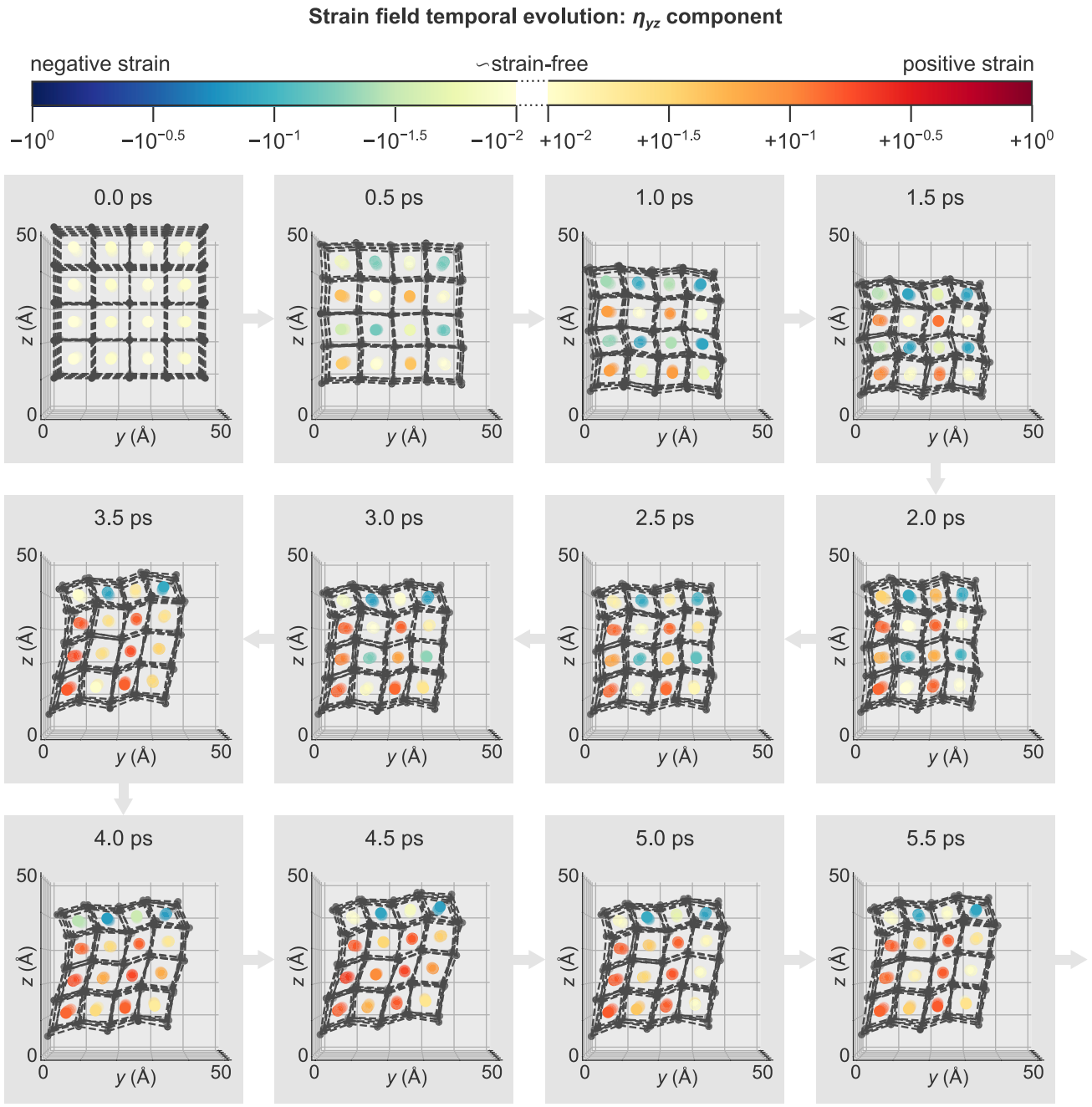

Figure 5. Temporal evolution of the inhomogeneous strain field in the strain-engineered UiO-66 material containing four linker vacancies
Shear (η_{yz}) strain field during the first 5.5 ps of applying a pressure of 1 GPa and at a temperature of 300 K. Throughout time, the two orthogonal instabilities first come to expression simultaneously, after which one of the horizontal shear instabilities is restored at this pressure.

under which a strain-engineered material exhibits a certain sought-after mechanical response or by introducing new mechanical responses in the strain-engineered material that are not present in the parent structure, as illustrated above for UiO-66. Having presented the strain fields generated in the six strain-engineered materials of Figure 1, we aim to demonstrate here that strain engineering is indeed a viable tool for designing such strain-engineered materials and rationalizing the origin of these anomalous properties.

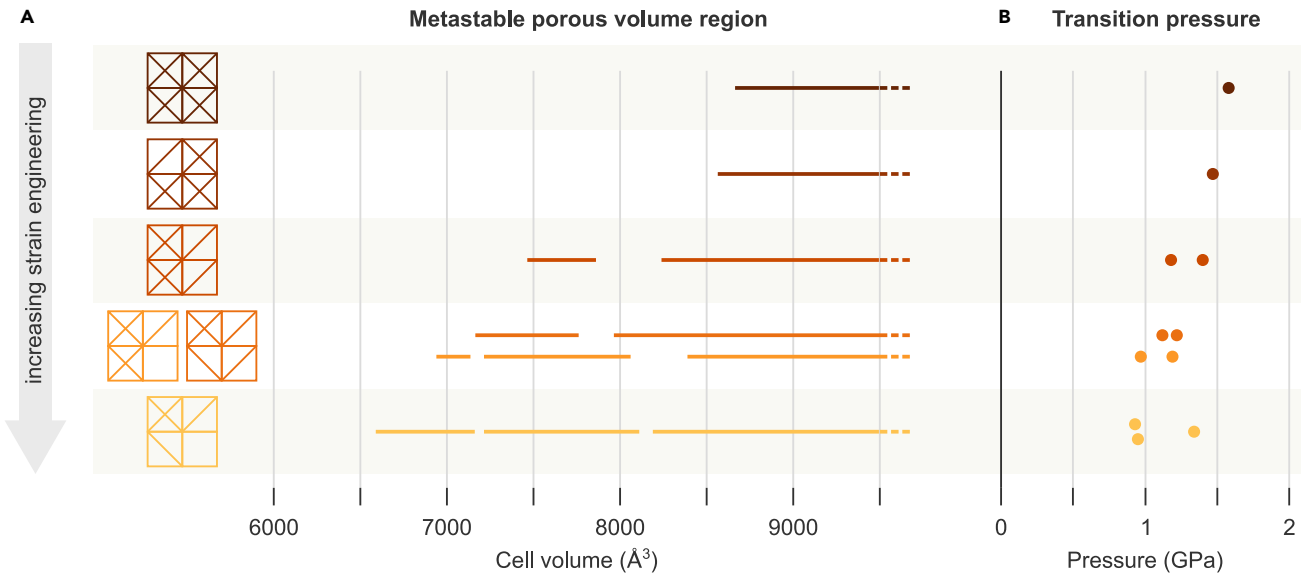

Figure 6. Overview of the volumes for which the strain-engineered UiO-66 materials are both stable and sufficiently porous, and the corresponding transition pressures of these materials

(A) Volume range for which each material is stable (as derived from a negative slope in the pressure-versus-volume equations of state) and exhibits a porosity exceeding 0.10 $cm^3\ g^{-1}$ for a probe particle of radius 1.2 Å.

(B) Transition pressures when compressing each of the different materials. For materials with multiple stable branches (see A), all transition pressures encountered upon increasing the pressure are reported. The two lowest transition pressures for the most defective material are vertically offset for clarity.

First, Figure 6A summarizes the stability results presented in Figures 2, 3, and 4, as well as in Figures S1–S3. More specifically, Figure 6A answers the question for which volume range the strain-engineered UiO-66 materials can be stabilized while simultaneously exhibiting sufficient porosity (using 0.10 $cm^3\ g^{-1}$ for a particle of radius 1.2 Å, such as hydrogen gas, as an arbitrary cutoff for the accessible gravimetric pore volume). We observe that strain engineering crumple zones in UiO-66 via shear instabilities allows us to design materials in which the stable, porous volume range is more than doubled upon compression compared with the defect-free material. This increase in interesting volume range comes at the expense of the critical pressure the material can withstand, as shown in Figure 6B. However, this trade-off is only minor, and the most defective material considered here can still accommodate a pressure of 0.93 GPa before the first crumple zone is activated. This balance between the pressure range over which a material is stable and the volume range over which it can be stabilized forms an interesting starting point to create either high-pressure shock absorbers or materials that can retain their porosity even for high pressures.

Besides these potential applications, Figure 6B also reveals that the synergistic interplay between different strain fields leads to an unexpected, anomalous effect in the critical pressure the material can withstand. Figure 6B contains all critical pressures found when gradually compressing a material starting from its equilibrium structure, as extracted from the pressure-versus-volume equations of state. To amorphize the material, a pressure higher than the maximum of these critical pressures should be applied. While one expects this pressure to decrease upon increased defectivity, Figure 6B demonstrates that this is not the case for the most defective material, in which the strain fields of two orthogonal shear instabilities interact. While the maximum critical pressure decreases from 1.58 GPa for the defect-free material to 1.19 GPa or 1.22 GPa for the materials containing three linker vacancies, this

maximum critical pressure increases again to at least 1.34 GPa for the most defective material considered here. This last value could be even higher given that the transition pressure to access the fourth and last metastable branch, in which all crumple zones are contracted, was not accessible during our simulations. The exact transition pressures depend slightly on the simulation cell size, which is not surprising because also the amount of crumple zones that can be activated in these materials is size dependent—similar to phase coexistence in soft porous crystals.[67] However, the supercell simulations reported in Note S3 indicate that the most defective material has a larger critical pressure than at least one of the two considered materials with one fewer linker vacancy also for 1×1×1 and 3×3×3 simulation cells.

The anomalous mechanical behavior identified here results from the interplay between two orthogonally induced crumple zones. While it has not yet been identified for framework materials, it is akin to Braess's paradox, initially encountered in traffic planning[68] but recently also proven to exist in electrical circuits.[69,70] In essence, Braess's paradox states that the efficiency of a network can be reduced rather than increased when adding components with extra capacity or, conversely, that the network's efficiency can be increased by removing components from it. For instance, adding an extra connection to an existing road network between two points may increase the time needed for each individual driver to travel between these two points if that driver chooses their route rationally.[68] This is a direct result of the presence of non-optimal equilibrium points in such a network; if all drivers in the previous example would collectively, rather than individually, select a route between the two points, the paradox would disappear. More recently, a similar paradox was predicted to occur in mesoscopic semiconductor networks, where the quantum transport in a two-branch network could be reduced by adding a third branch, as manifested through a sizable drop in the conductance of the network.[69] Our results indicate that a similar paradox may also occur for the mechanical stability of a material—a consequence of the occurrence of two equivalent orthogonal crumple zones between which must be chosen to compress the material—although its actual existence remains to be proven experimentally.

Generalization of strain engineering toward other materials and strain triggers

For strain engineering to form a generally applicable approach for materials design, it is vital to show that it is equally applicable to other materials and other thermodynamic stimuli besides the pressure-induced flexibility introduced in UiO-66(Zr). To this end, we here investigate CoBDP.[71] CoBDP is a soft porous crystal that switches between different phases upon external stimuli, such as gas adsorption, contrasting with the rigid UiO-66(Zr) framework investigated before. Our earlier work predicted that multiple phases could coexist in a layer-by-layer fashion in CoBDP under specific thermodynamic conditions.[67] Furthermore, we hypothesized that such phase coexistence states could be reached by judiciously controlling the methane adsorption in this material.[67] Compared to our aforementioned strain engineering predictions for UiO-66, for which the actual experimental realization of flexibility depends on the synthetic feasibility of introducing specific linker vacancies, CoBDP may form an experimentally more accessible approach to demonstrate, through gas adsorption, how strain fields can help to rationalize intriguing material phenomena.

To this end, Figure 7 visualizes how methane adsorption alters the occurrence of phase coexistence in CoBDP. The pressure-versus-volume equation of state corresponding to the empty framework in Figure 7B reveals multiple metastable branches, which we denoted by the (n_{cp}, n_{lp}) label to indicate how many closed-pore

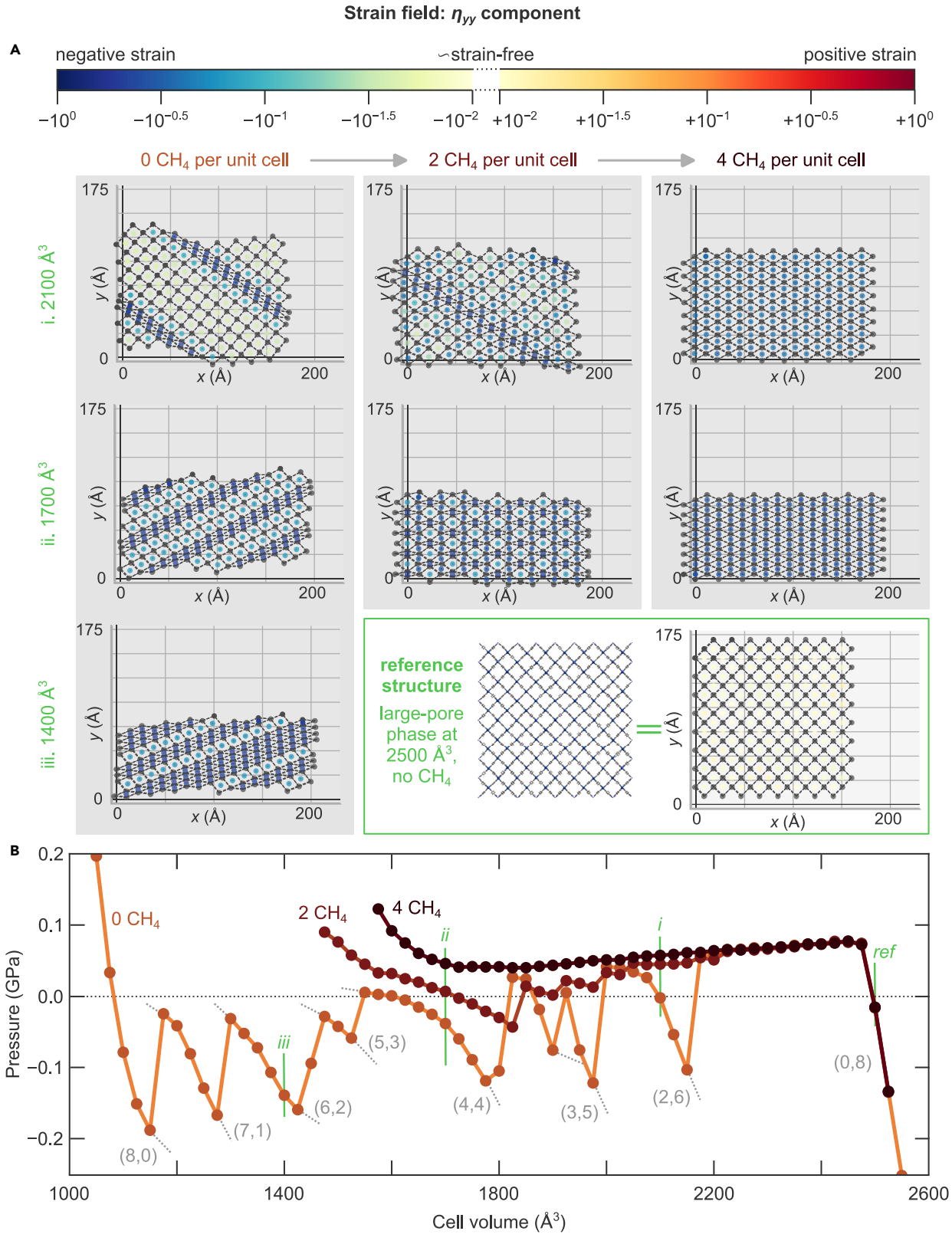
Strain field: η_{yy} component
A
negative strain
strain-free
positive strain
-10^{0}
$-10^{-0.5}$
-10^{-1}
$-10^{-1.5}$
-10^{-2}
$+10^{-2}$
$+10^{-1.5}$
$+10^{-1}$
$+10^{-0.5}$
$+10^{0}$
0 CH_4 per unit cell
2 CH_4 per unit cell
4 CH_4 per unit cell
i. 2100 Å^3
ii. 1700 Å^3
iii. 1400 Å^3
y (Å)
x (Å)
reference structure
large-pore phase at 2500 Å^3, no CH_4
B
Pressure (GPa)
Cell volume (Å^3)
0 CH_4
2 CH_4
4 CH_4
i
ii
iii
ref
(8,0)
(7,1)
(6,2)
(5,3)
(4,4)
(3,5)
(2,6)
(0,8)

Figure 7. Strain fields reveal the impact of methane adsorption on phase coexistence in the flexible CoBDP material

(A) Reference atomic structure of the 8×8×2 simulation cell and uniaxial (η_{yy}) strain fields at three selected volumes and three different methane loadings (0, 2, and 4 methane molecules per unit cell), demonstrating that methane adsorption smears out the strain over the material and hence disfavors phase coexistence. The strain present in each region is color coded from yellow (low strain) to either blue (large negative strain) or red (large positive strain).

(B) Pressure-versus-volume equations of state at 300 K, with the structures found in (A) (green lines, numbered i to iii) and the different (n_{cp}, n_{lp}) metastable branches indicated. (B) was adapted from Rogge et al.[67] with permission from the Nature Publishing Group.

(cp) and large-pore (lp) layers coexist in the structure. In total, eight such metastable branches exist. As observed in Rogge et al.,[67] these metastable branches partially or wholly disappear upon adsorbing two and four methane molecules per unit cell, respectively. At that moment, the origin of this effect was only attributed to the destabilization of the cp phase upon gas adsorption, which is, for instance, evident in Figure 7B by the relatively larger pressures required to compress the methane-loaded material to volumes below ca. 1,600 Å^3 compared with the empty framework. We will here demonstrate that our strain field approach reveals a more detailed explanation that complements this earlier observation.

The first column of Figure 7A visualizes the η_{yy} strain fields arising in the empty CoBDP framework at representative unit cell volumes of 1,400 Å^3, 1,700 Å^3, and 2,100 Å^3, using the lp structure at 2,500 Å^3 as the reference structure. Upon pressurization, different cp layers start to coexist together with the original lp layers, leading to (2,6) phase coexistence in structure i, (4,4) phase coexistence in structure ii, and (6,2) phase coexistence in structure iii. In each case, the cp layers exhibit a negative η_{yy} strain about one order of magnitude larger in amplitude than the strain in the lp layers. Similar to our crumple zone observations in UiO-66, the cp layers locally focus the strain, although the phase coexistence regions are triggered at much lower pressures than the crumple zones in UiO-66. Given the typical winerack motion in CoBDP, these negative η_{yy} strains correspond to positive η_{xx} strains, which could also be used to visualize phase coexistence. Interestingly, the strain field of the empty structure i evidences the existence of a buffer layer between the lp and cp layers. Based on their volume, the cells in these buffer layers are close to the lp state, although they exhibit substantially more strain than the lp cells located further away from the cp layers.

Upon methane adsorption, the strain fields change substantially. A loading of two methane molecules per unit cell already prevents phase coexistence to manifest at low volumes such as for structure iii, which can be explained by the aforementioned destabilization of the cp phase. In addition, the strain fields of the loaded structures differ from the corresponding unloaded structures also for the larger volumes in structures i and ii, which cannot be explained by cp phase destabilization alone. For instance, at two methane molecules per unit cell, structure ii shows a more homogeneous—yet still layer-by-layer—distribution of lp and cp cells. Even more prominently, the strain in structure i not only focuses along one main diagonal (from top left to bottom right in the figure) but also produces a wave-like pattern along the opposite diagonal in which the strain in the lp cells alternates between nearly inexistent and up to $\eta_{yy} = -0.1$. Upon further adsorption, the layer-by-layer coexistence completely disappears at four methane molecules per unit cell and is replaced by a homogeneous strain field throughout the material. Based on these observations, methane adsorption not only destabilizes the cp phase, as argued before, but also acts as a strain trigger in itself that redistributes and homogenizes the strain inside the empty host. This strain redistribution disfavors the occurrence of phase coexistence for the methane-loaded systems, also at larger volumes. A similar redistribution and homogenization effect also arises when adsorbing methane in the defective UiO-66(Zr) materials, as demonstrated in Note S4.

Interestingly, in the UiO-66 case, this redistribution only affects the crumple zones, preserving the rigidity of the remainder of the material. Hence, gas adsorption forms a potential pathway to alter the strain fields in these structures.

To further expand the scope of strain engineering and provide potential avenues to experimentally realize the here-proposed strain fields under different thermodynamic triggers, two additional materials for which we predicted earlier how to induce phase coexistence are considered in Note S5.[67] For the pressure-induced phase coexistence in DMOF-1(Zn),[72] the strain fields derived here reveal that buffer layers exist between the lp and cp layers. Akin to our observation in CoBDP structure i of Figure 7, the cells in these buffer layers are closer to the lp volume but exhibit about one order of magnitude larger strain than the other lp layers. A similar buffer layer arises for the temperature-induced phase coexistence in MIL-53(Al)-F.[73] In addition, comparing the strain fields arising in the MIL-53(Al)-F structure at 100 K, 300 K, and 500 K reveals that increasing the temperature redistributes and homogenizes the strain fields in the material, similar to the adsorption of methane in CoBDP. This explains why phase coexistence in this material only occurs at sufficiently low temperatures. A homogeneous phase between the cp and lp phases with a homogeneous strain distribution is preferred at higher temperatures.

DISCUSSION

In this work, we introduced the concept of strain engineering for nanostructured materials to rationalize the causal impact of atomic-level alterations in these structures on their macroscopic mechanical properties and to exploit this information to design materials with unexpected yet attractive phenomena. As a case study, we firstly focused on UiO-66, a rigid material that amorphizes irreversibly when too large a pressure is applied. By incorporating two linker vacancies in the material to introduce a potential shear instability, we substantially expanded the volume range for which the now locally flexible material remains mechanically stable. In addition, we showed that it retains, at least partially, its porosity at the expense of a slight reduction in the critical pressure needed to amorphize the material. This observation was rationalized through strain fields, which are spatially and temporally varying tensor fields that lay at the heart of strain engineering. These strain fields demonstrate that the shear instability introduced in the structure acts as a molecular crumple zone in which the strain is concentrated. In contrast, the remainder of the material remains, comparatively, almost strain free.

Subsequently, this observation was taken a step further by strain engineering a second orthogonal crumple zone in the UiO-66 material by removing four linkers. The material strain engineered with two such orthogonal crumple zones remains mechanically stable over an expanded volume range. Remarkably, the sacrificial volume for which the porosity is lost when the crumple zones are activated does not increase appreciably compared with the material with only a single crumple zone. This observation is a direct result of the fact that, at the intersection between these two crumple zones, the shear stresses have an opposite sign and virtually cancel out. As a result, our strain engineering approach demonstrates that the two strain fields introduced by these crumple zones interact synergistically.

Our strain-engineered UiO-66 materials show promise for shock absorption or adsorption applications under a mechanical pressure thanks to their extended stability. Additionally, we also revealed two mechanical anomalies that, if confirmed experimentally, would further expand the application domain of nanostructured

framework materials. Firstly, we predicted that the introduction of crumple zones would pave the way to create locally flexible materials, thereby forming a continuum in design space between completely rigid materials and those that are completely flexible—the so-called soft porous crystals. Secondly, our simulations predicted that the UiO-66 material strain engineered with two orthogonal crumple zones exhibits a higher amorphization pressure than its less defective parent material containing one fewer linker vacancy. This counterintuitive effect is akin to Braess's paradox in traffic flow and electrical circuits and would be the first example of a mechanical analog of this paradox.

Finally, to illustrate the broad applicability of strain engineering in terms of materials and thermodynamic triggers, we focused our attention on investigating how thermodynamic stimuli affect the phase coexistence in CoBDP and other soft porous crystals. Our strain engineering approach highlighted that the cp layers in these materials focus the strain while keeping the lp layers largely strain free, similar to the role of crumple zones in UiO-66. In addition, this approach revealed two new insights into these materials. Firstly, it points toward the existence of buffer layers between the earlier observed lp and cp layers. While the cells in these buffer layers are characterized by volumes close to the lp phase, they exhibit about one order of magnitude larger strains than the other lp cells. Secondly, both methane adsorption (for CoBDP) and increases in temperature (for MIL-53(Al)-F) are triggers to homogenize the strain field in these materials, thereby counteracting the tendency to form layer-by-layer phase coexistence. These strain engineering insights explain why phase coexistence is preferentially found in empty frameworks and at lower temperatures and complement our earlier rationalization for phase coexistence. They demonstrate that strain fields emerging in a material strongly depend on the thermodynamic conditions under which the material is maintained. These additional examples also serve as an experimentally more accessible approach to designing strain fields in MOFs, given that the introduction of well-defined linker vacancies in UiO-66(Zr) may remain an experimental challenge at the moment.

The present work reveals that the here-introduced strain engineering approach fulfills the two necessary criteria for any design tool. Strain engineering can (1) isolate causal relationships between atomic-level alterations and their impact on the macroscopic mechanical behavior of the material and (2) predict how different such alterations cooperatively impact one another. At the moment, our approach is limited mainly by the restrictions in the model sizes that can be simulated to investigate the cooperativity of strain fields, as well as by the accuracy with which the interactions in these materials are modeled, especially for larger models. In addition, since our strain fields rely on the definition of a proper reference cell, it is crucial to identify the atomic structure of this cell, which can be challenging, especially for amorphous structures. These limitations define important research avenues that may substantially broaden the applicability of the here-presented concept and of materials science in general. Finally, as mentioned before, the strain engineering concept introduced in this work is—so far—a theoretical concept with the potential to be realized experimentally. Given the length- and timescales on which we here predicted strain fields, realizing and visualizing these strain fields experimentally remain open and challenging research questions, as this requires dedicated techniques with a high spatiotemporal resolution that do not interfere with the strain fields themselves. However, even with these current limitations, the strain engineering domain of application potentially goes far beyond what we demonstrated here. Since strain engineering only requires a decomposition of the complete material in a non-overlapping grid of

parallelepipeds, it is equally applicable to MOFs, COFs, and perovskites. As it is a dimensionless metric, the strain distribution in different materials—even if they are chemically completely distinct—can be easily and consistently compared, resulting in a material-transcending design tool. Furthermore, it can be used both in conjunction with classical force fields or by using density functional theory or other reactive levels of theory if bonds reorganize in the process. Therefore, strain engineering has the potential to fundamentally shape the design of these functional materials as a general and transferable design tool in materials science.

EXPERIMENTAL PROCEDURES

Resource availability

Lead contact

Further information and requests for resources and materials should be directed to and will be fulfilled by the lead contact, Sven M.J. Rogge (Sven.Rogge@UGent.be).

Materials availability

This study did not generate new, unique reagents.

Data and code availability

Computational data supporting the results of this work are available from Zenodo under https://doi.org/10.5281/zenodo.7577607 and from the GitHub repository at https://github.com/SvenRogge/supporting-info.

Representative input and processing scripts for the used software code are available from Zenodo under https://doi.org/10.5281/zenodo.7577607 and from the GitHub repository at https://github.com/SvenRogge/supporting-info.

Any additional information required to reanalyze the data reported in this paper is available from the lead contact upon request.

Strain field generation

To visualize the UiO-66 strain fields in this article, we first determined the center of mass positions of each inorganic zirconium building block in the 2×2×2 supercell, yielding 32 time-dependent positions. Subsequently, an additional 32 time-dependent positions representing the centers of the octahedral pores of the material were calculated by taking the means of the positions of the six inorganic building blocks defining this octahedron. Periodic boundary conditions were taken into account whenever necessary. As a result, a time-dependent 4×4×4 grid of positions $\{\boldsymbol{r}_{ijk}(t)\}$ is generated in which the locations of the inorganic building blocks alternate with the locations of the centers of the octahedral pores, as indicated schematically in Figure 8A.

The 4×4×4 grid of positions was then used to construct a time-dependent 4× 4× 4 grid of parallelepipeds with matrices $\{\mathbf{h}_{\mu\nu\kappa}(t)\}$ whose vertices maximally coincide with the 4×4×4 grid of positions following the procedure outlined in Figures 8B and 8C. To this end, consider an arbitrary cell at index (μ, ν, κ), which is delineated by eight vertices in the 4×4×4 grid of positions. The twelve edges of this cell are formed by the relative vectors between pairs of adjacent vertices, as shown by the dashed lines in Figure 8B. In a true parallelepiped, these twelve relative vectors would consist of three groups, each composed of four identical vectors, as indicated by the three colors. In reality, however, each node can move independently. An average relative vector is constructed by averaging within each of the three groups over the four vectors that would be identical in a true parallelepiped. This procedure results in the best-fitting parallelepiped of Figure 8C. Finally, these three average relative vectors are stored in

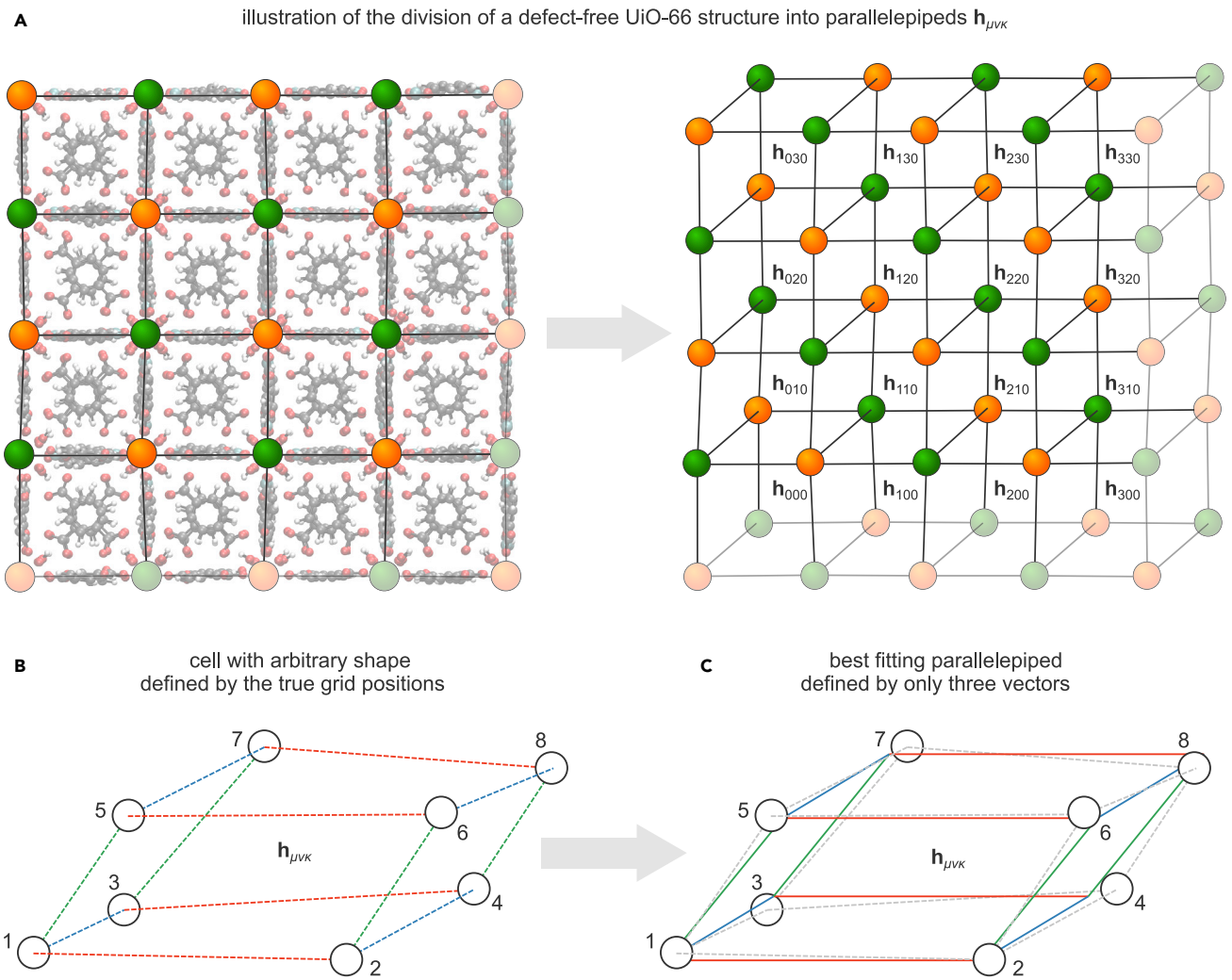

Figure 8. Procedure to generate a grid of cell matrices $\{\mathbf{h}_{\mu\nu\kappa}\}$ from a grid of positions $\{\mathbf{r}_{ijk}\}$

(A) Consider, as an example, a 2×2× 2 supercell of the defect-free UiO-66(Zr) structure. Based on the positions of all atoms, this structure will be divided into a 4×4× 4 array of non-overlapping cells. To this end, define on the one hand the centers of each of the 32 Zr bricks, indicated by orange spheres, and on the other hand the centers of each of the 32 octahedral pores in the material, indicated by green spheres (semitransparent spheres correspond to periodic images). These 64 positions $\mathbf{r}_{ijk}$, with $i,j,k \in \{0,1,2,3\}$, define the sought-after array of cells $\mathbf{h}_{\mu\nu\kappa}$ (with $\mu,\nu,\kappa \in \{0,1,2,3\}$), as illustrated in the top right figure for the first layer of cells (with K = 0).

(B) Now consider eight vertices, numbered 1 to 8, at positions $\mathbf{r}_{ijk}$ that delineate the cell at the arbitrary index (μ,ν,κ). Since the positions of these vertices vary freely during a simulation, the cell's shape is completely free. To assign a parallelepiped and hence a cell matrix $\mathbf{h}_{\mu\nu\kappa}$ to this arbitrary cell, the average is taken over all equally colored vectors in (B).

(C) Resulting parallelepiped that best fits the eight vertices. The vectors spanning this parallelepiped are stored in the rows of the cell matrix $\mathbf{h}_{\mu\nu\kappa}$, which is then used to calculate the strain through Equation 1. The deviations of the vertices from a true parallelepiped are exaggerated here for visualization.

the rows of the matrix $\mathbf{h}_{\mu\nu\kappa}$. This procedure is repeated for each cell along the grid and each time step to yield the complete set of parallelepipeds, $\{\mathbf{h}_{\mu\nu\kappa}(t)\}$.

By repeating this procedure for each time step and each cell present in the 4× 4× 4 grid, the space- and time-dependent strain fields visualized in Figures 2, 3, 4, and 5, as well as in Figures S1–S3 and S6, are constructed through Equation 1. The reference cell $\mathbf{h}_{\mathrm{ref},\mu\nu\kappa}$ in this equation is the same at each time instant and for each cell within a given material and corresponds to the equilibrium structure at 300 K and 0 MPa, shown as structure i in Figures 2A, 3A, and 4A. Finally, the strain field is

visualized together with the positions of the 64 vertices and the edges connecting them. For those vertices at the boundaries of the simulation cell, both the vertex itself and its periodic image are shown for visualization purposes.

For the soft porous crystals described in Figures 7, S7, and S8, a similar approach was adopted to construct 8×8×2 strain grids. The short axis corresponds to the "rigid" pillar of these pillared-layered materials. The 8×8×2 grid of positions denoting the vertices of the different parallelepipeds was formed by the centers of mass of two adjacent cobalt atoms (for CoBDP), the centers of mass of the zinc paddlewheel units (for DMOF-1(Zn)), or the centers of mass of two adjacent aluminum atoms (for MIL-53(Al)-F). The cells taken as reference structures are denoted in each of the different pressure-versus-volume equations of state.

Pressure-versus-volume equations of state

The pressure-versus-volume equations of state reported in Figures 2B, 3B, 4B, and 7B, as well as in Figures S1–S8, predict for a predefined range of volumes the average internal pressure the material exerts on its environment.[74] As this internal pressure equals the external pressure in mechanical equilibrium, these equations of state predict the evolution of a system under the application of either a constant pressure or a more complex pressure treatment, with an improved accuracy with respect to traditional constant-pressure simulations.[75] A pressure-versus-volume equation of state can be separated into volume regions with a distinctly different behavior based on the local $\partial P/\partial V$ slope of the profile. Given that the negative of this slope is proportional to the bulk modulus, volume regions for which $\partial P/\partial V > 0$ are mechanically unstable. They separate mechanically stable regions for which $\partial P/\partial V < 0$. These mechanically stable regions can be thermodynamically stable or metastable and are accessible through experiments if they correspond to positive pressures. Mechanically stable and unstable regions are separated by maxima and minima in the equations of state. These maxima and minima therefore correspond to critical pressures, i.e., the pressure one needs to apply to force the system to transition from one mechanically stable region to another mechanically stable region, thereby crossing a mechanically unstable volume range, as in an experimental compression or decompression experiment. The pressure-versus-volume equations of state are also used to find the equilibrium structures at the specified thermodynamic conditions, namely by determining the intersection between this pressure profile and the horizontal at 0 MPa.

The equations of state are constructed based on the methodology established in Rogge et al.[74] and is here illustrated for the UiO-66 simulations. In short, a range of volumes is predefined—here between 6,000 Å^3 and 9,500 Å^3 with a step size of 25 Å^3. For each volume, an initial structure is obtained based on a prior $(N, P, \boldsymbol{\sigma}_a = \mathbf{0}, T)$ simulation at the required temperature T (here 300 K) and at a pressure P that is appropriate to encounter the required volume during the molecular dynamics (MD) simulation. Then, for each volume separately, that structure is used to initialize an $(N, V, \boldsymbol{\sigma}_a = \mathbf{0}, T)$ simulation, in which the number of particles N and the volume V are kept constant. In contrast, the deviatoric stress $\boldsymbol{\sigma}_a$ and the temperature T are controlled to be 0 and 300 K, respectively, using a thermostat and a barostat (*vide infra*).[74] In this way, during the simulation, all degrees of freedom except for the volume—i.e., the atomic degrees of freedom as well as the cell shape—are allowed to adapt themselves to the external conditions. From these MD simulations, the average internal pressure at each volume point can be constructed, yielding the pressure-versus-volume equations of state reported in Figures 2B, 3B, and 4B, as well as in Figures S1–S3. The robustness of this protocol, especially given the

occurrence of different metastable branches, is further discussed in Note S2. A similar procedure is used for the soft porous crystals, as detailed in Rogge et al.[67]

Force-field derivation

To describe the interatomic interactions in the UiO-66 materials described in this work, flexible and system-specific force fields were derived for each of the six materials in Figure 1 using the QuickFF methodology.[76,77] To this end, the Hessian and equilibrium geometries extracted from the *ab initio* calculations reported in Rogge et al.[56] on the four distinct building blocks of Figure 1—the organic linker as well as the three different zirconium building blocks—were used to construct cluster-based force fields. They were then appropriately combined to obtain a system-specific, periodic force field for each of the six different materials. Besides the efficiency of this building block approach, it also ensures maximum transferability between the different periodic structures considered here. The electrostatic interactions between two atoms are described by the Coulomb interaction between Gaussian charge distributions, for which the charges are derived from the *ab initio* electron density of each model system. The charge radii are based on the fitting procedure of Chen and Martinéz.[78] Charges from the cluster calculations are transferred to the periodic structures via bond-charge increments.[79] The van der Waals interactions are modeled based on the two-parameter MM3 Buckingham potential,[80] using the Lorentz-Berthelot mixing rules. The covalent force fields do not contain cross terms. All force fields are available at https://github.com/SvenRogge/supporting-info. The simulations reported in Rogge et al.[67] were adopted to visualize the strain fields for the soft porous crystals. No new force fields were derived for these materials.

Two specific improvements have been made for the UiO-66 force fields compared with the original formulation in Rogge et al.[56] Firstly, more specific atom types were introduced for the carboxylate oxygens that connect the inorganic and the organic brick. This ensures that those carboxylate oxygens are assigned distinct atom types if they lie in different planes. This allows for the necessary freedom in the force field to reproduce the interactions, as the angle between these carboxylate oxygens as seen from the zirconium atom they connect is different when the carboxylate oxygens are in different planes. Secondly, force constants were averaged over similar force-field terms to keep the force field interpretable and transferable. As discussed in Note S6, this leads to an improved reproduction of the interatomic interactions compared with Rogge et al.[56]

MD simulation and visualization details

All UiO-66 MD simulations, whether in the $(N, V, \boldsymbol{\sigma}_a = \mathbf{0}, T)$ ensemble (for the pressure-versus-volume equations of state) or the $(N, P, \boldsymbol{\sigma}_a = \mathbf{0}, T)$ ensemble, were carried out on a 2×2×2 supercell of the conventional unit cell using our in-house developed software code Yaff.[81] The only exceptions are the different simulation box sizes investigated in Note S3. Our code was interfaced with LAMMPS to efficiently calculate the long-range, non-covalent interactions.[82] During these MD simulations, the temperature was controlled using a Nosé-Hoover chain thermostat consisting of three beads and with a time constant of 0.1 ps,[83–86] whereas the stress was controlled with a Martyna-Tobias-Klein barostat with a time constant of 1 ps.[87,88] The velocity Verlet scheme was adopted to integrate the equations of motion, using a time step of 0.5 fs to ensure energy conservation, until a total simulation time of 1 ns was reached. The long-range van der Waals interactions were cut off at a radius of 12 Å, which was compensated by tail corrections. The electrostatic interactions were efficiently calculated using an Ewald summation with a real-space cutoff of 12 Å, a splitting parameter α of 0.213 $Å^{-1}$, and a reciprocal space cutoff of 0.32 $Å^{-1}$.[89]

The atomic structures displayed in this work were generated using either iRASPA (for the graphical abstract)[90] or VMD,[91] whereas the volume-dependent accessible pore volume analyses shown in Figures 2C, 3C, and 4C, as well as in Figures S1–S3, were calculated with Zeo++ using a spherical probe with radius 1.2 Å.[92]

SUPPLEMENTAL INFORMATION

Supplemental information can be found online at https://doi.org/10.1016/j.matt.2023.02.009.

ACKNOWLEDGMENTS

This work is supported by the Fund for Scientific Research Flanders (FWO) through a postdoctoral fellowship for S.M.J.R. (grant no. 12T3522N) and the Research Board of Ghent University (BOF) through a Concerted Research Action (GOA010-17) and the Special Research Fund of Ghent University (iBOF-21-085 PERsist). V.V.S acknowledges funding from the Research Board of Ghent University (BOF). The computational resources and services used in this work were provided by the VSC (Flemish Supercomputer Center), funded by the Research Foundation—Flanders (FWO) and the Flemish Government – department EWI. We thank Professor A.L. Goodwin for stimulating discussions on the topic.

AUTHOR CONTRIBUTIONS

S.M.J.R., S.B., and V.V.S. initiated the discussion. S.B. derived the different force fields. S.M.J.R. designed the strain engineering protocol and performed the MD simulations. All authors designed the paper and were involved in the analysis and discussion of the results. S.M.J.R. wrote the manuscript with contributions of all authors.

DECLARATION OF INTERESTS

The authors declare no competing interests.

INCLUSION AND DIVERSITY

We support inclusive, diverse, and equitable conduct of research.

Received: July 27, 2022
Revised: January 6, 2023
Accepted: February 14, 2023
Published: March 13, 2023

REFERENCES

1. Yaghi, O.M., O'Keeffe, M., Ockwig, N.W., Chae, H.K., Eddaoudi, M., and Kim, J. (2003). Reticular synthesis and the design of new materials. Nature *423*, 705–714. https://doi.org/10.1038/nature01650.

2. Freund, R., Canossa, S., Cohen, S.M., Yan, W., Deng, H., Guillerm, V., Eddaoudi, M., Madden, D.G., Fairen-Jimenez, D., Lyu, H., et al. (2021). 25 years of reticular chemistry. Angew. Chem. Int. Ed. Engl. *60*, 23946–23974. https://doi.org/10.1002/anie.202101644.

3. Zhang, B., Mao, H., Matheu, R., Reimer, J.A., Alshmimri, S.A., Alshihri, S., and Yaghi, O.M. (2019). Reticular synthesis of multinary covalent organic frameworks. J. Am. Chem. Soc. *141*, 11420–11424. https://doi.org/10.1021/jacs.9b05626.

4. Steele, J.A., Prakasam, V., Huang, H., Solano, E., Chernyshov, D., Hofkens, J., and Roeffaers, M.B.J. (2021). Trojans that flip the black phase: impurity-driven stabilization and spontaneous strain suppression in γ-$CsPbI_3$ perovskite. J. Am. Chem. Soc. *143*, 10500–10508. https://doi.org/10.1021/jacs.1c05046.

5. Krause, S., Bon, V., Senkovska, I., Stoeck, U., Wallacher, D., Többens, D.M., Zander, S., Pillai, R.S., Maurin, G., Coudert, F.-X., et al. (2016). A pressure-amplifying framework material with negative gas adsorption transitions. Nature *532*, 348–352. https://doi.org/10.1038/nature17430.

6. Krause, S., Evans, J.D., Bon, V., Senkovska, I., Iacomi, P., Kolbe, F., Ehrling, S., Troschke, E., Getzschmann, J., Többens, D.M., et al. (2019). Towards general network architecture design criteria for negative gas adsorption transitions in ultraporous frameworks. Nat. Commun. *10*, 3632. https://doi.org/10.1038/s41467-019-11565-3.

7. Protesescu, L., Yakunin, S., Bodnarchuk, M.I., Krieg, F., Caputo, R., Hendon, C.H., Yang, R.X., Walsh, A., and Kovalenko, M.V. (2015). Nanocrystals of cesium lead halide perovskites ($CsPbX_3$, X = Cl, Br, and I): novel optoelectronic materials showing bright emission with wide color gamut. Nano Lett. *15*, 3692–3696. https://doi.org/10.1021/nl5048779.

8. Akkerman, Q.A., D'Innocenzo, V., Accornero, S., Scarpellini, A., Petrozza, A., Prato, M., and Manna, L. (2015). Tuning the optical properties of cesium lead halide perovskite nanocrystals by anion exchange reactions. J. Am. Chem. Soc. *137*, 10276–10281. https://doi.org/10.1021/jacs.5b05602.

9. Maurin, G., Serre, C., Cooper, A., and Férey, G. (2017). The new age of MOFs and of their porous-related solids. Chem. Soc. Rev. *46*, 3104–3107. https://doi.org/10.1039/C7CS90049J.

10. Dincă, M., and Long, J.R. (2020). Introduction: porous framework chemistry. Chem. Rev. *120*, 8037–8038. https://doi.org/10.1021/acs.chemrev.0c00836.

11. Furukawa, H., Cordova, K.E., O'Keeffe, M., and Yaghi, O.M. (2013). The chemistry and applications of metal–organic frameworks. Science *341*, 1230444. https://doi.org/10.1126/science.1230444.

12. Geng, K., He, T., Liu, R., Dalapati, S., Tan, K.T., Li, Z., Tao, S., Gong, Y., Jiang, Q., and Jiang, D. (2020). Covalent organic frameworks: design, synthesis, and functions. Chem. Rev. *120*, 8814–8933. https://doi.org/10.1021/acs.chemrev.9b00550.

13. Troyano, J., Legrand, A., and Furukawa, S. (2021). Mechanoresponsive porosity in metal-organic frameworks. Trends Chem. *3*, 254–265. https://doi.org/10.1016/j.trechm.2021.01.004.

14. Ablitt, C., Craddock, S., Senn, M.S., Mostofi, A.A., and Bristowe, N.C. (2017). The origin of uniaxial negative thermal expansion in layered perovskites. npj Comput. Mater. *3*, 44. https://doi.org/10.1038/s41524-017-0040-0.

15. Coudert, F.-X., and Evans, J.D. (2019). Nanoscale metamaterials: meta-MOFs and framework materials with anomalous behavior. Coord. Chem. Rev. *388*, 48–62. https://doi.org/10.1016/j.ccr.2019.02.023.

16. Vanduyfhuys, L., Rogge, S.M.J., Wieme, J., Vandenbrande, S., Maurin, G., Waroquier, M., and Van Speybroeck, V. (2018). Thermodynamic insight into stimuli-responsive behaviour of soft porous crystals. Nat. Commun. *9*, 204. https://doi.org/10.1038/s41467-017-02666-y.

17. Cairns, A.B., and Goodwin, A.L. (2015). Negative linear compressibility. Phys. Chem. Chem. Phys. *17*, 20449–20465. https://doi.org/10.1039/C5CP00442J.

18. Huang, C.W., Ren, W., Nguyen, V.C., Chen, Z., Wang, J., Sritharan, T., and Chen, L. (2012). Abnormal Poisson's ratio and linear compressibility in perovskite materials. Adv. Mater. *24*, 4170–4174. https://doi.org/10.1002/adma.201104676.

19. Ryder, M.R., and Tan, J.-C. (2016). Explaining the mechanical mechanisms of zeolitic metal–organic frameworks: revealing auxeticity and anomalous elasticity. Dalton Trans. *45*, 4154–4161. https://doi.org/10.1039/C5DT03514G.

20. Kapustin, E.A., Lee, S., Alshammari, A.S., and Yaghi, O.M. (2017). Molecular retrofitting adapts a metal–organic framework to extreme pressure. ACS Cent. Sci. *3*, 662–667. https://doi.org/10.1021/acscentsci.7b00169.

21. Schneider, C., Bodesheim, D., Keupp, J., Schmid, R., and Kieslich, G. (2019). Retrofitting metal–organic frameworks. Nat. Commun. *10*, 4921. https://doi.org/10.1038/s41467-019-12876-1.

22. Steele, J.A., Jin, H., Dovgaliuk, I., Berger, R.F., Braeckevelt, T., Yuan, H., Martin, C., Solano, E., Lejaeghere, K., Rogge, S.M.J., et al. (2019). Thermal unequilibrium of strained black $CsPbI_3$ thin films. Science *365*, 679–684. https://doi.org/10.1126/science.aax3878.

23. Simonov, A., and Goodwin, A.L. (2020). Designing disorder into crystalline materials. Nat. Rev. Chem *4*, 657–673. https://doi.org/10.1038/s41570-020-00228-3.

24. Bratkovsky, A.M., Salje, E.K.H., Marais, S.C., and Heine, V. (1995). Strain coupling as the dominant interaction in structural phase transitions. Phase Transitions *55*, 79–126. https://doi.org/10.1080/01411599508200427.

25. Putnis, A. (2008). An Introduction to Mineral Sciences (Cambridge University Press).

26. Hobday, C.L., and Kieslich, G. (2021). Structural flexibility in crystalline coordination polymers: a journey along the underlying free energy landscape. Dalton Trans. *50*, 3759–3768. https://doi.org/10.1039/D0DT04329J.

27. Fang, Z., Bueken, B., De Vos, D.E., and Fischer, R.A. (2015). Defect-engineered metal-organic frameworks. Angew. Chem. Int. Ed. Engl. *54*, 7234–7254. https://doi.org/10.1002/anie.201411540.

28. Shearer, G.C., Chavan, S., Bordiga, S., Svelle, S., Olsbye, U., and Lillerud, K.P. (2016). Defect engineering: tuning the porosity and composition of the metal–organic framework UiO-66 via modulated synthesis. Chem. Mater. *28*, 3749–3761. https://doi.org/10.1021/acs.chemmater.6b00602.

29. Van Speybroeck, V., Vandenhaute, S., Hoffman, A.E.J., and Rogge, S.M.J. (2021). Towards modeling spatiotemporal processes in metal–organic frameworks. Trends Chem. *3*, 605–619. https://doi.org/10.1016/j.trechm.2021.04.003.

30. Arzt, E. (1998). Size effects in materials due to microstructural and dimensional constraints: a comparative review. Acta Mater. *46*, 5611–5626. https://doi.org/10.1016/S1359-6454(98)00231-6.

31. Arzt, E., and Wilkinson, D.S. (1986). Threshold stresses for dislocation climb over hard particles: the effect of an attractive interaction. Acta Metall. *34*, 1893–1898. https://doi.org/10.1016/0001-6160(86)90247-6.

32. Thompson, C.V. (2000). Structure evolution during processing of polycrystalline films. Annu. Rev. Mater. Sci. *30*, 159–190. https://doi.org/10.1146/annurev.matsci.30.1.159.

33. von Blanckenhagen, B., Gumbsch, P., and Arzt, E. (2003). Dislocation sources and the flow stress of polycrystalline thin metal films. Philos. Mag. Lett. *83*, 1–8. https://doi.org/10.1080/0950083021000050287.

34. Yu, H.Z., and Thompson, C.V. (2015). Stress engineering using low oxygen background pressures during Volmer–Weber growth of polycrystalline nickel films. J. Vac. Sci. Technol. A *33*, 021504. https://doi.org/10.1116/1.4902957.

35. Rogge, S.M.J. (2021). The micromechanical model to computationally investigate cooperative and correlated phenomena in metal–organic frameworks. Faraday Discuss. *225*, 271–285. https://doi.org/10.1039/C9FD00148D.

36. Liu, L., Chen, Z., Wang, J., Zhang, D., Zhu, Y., Ling, S., Huang, K.-W., Belmabkhout, Y., Adil, K., Zhang, Y., et al. (2019). Imaging defects and their evolution in a metal-organic framework at sub-unit-cell resolution. Nat. Chem. *11*, 622–628. https://doi.org/10.1038/s41557-019-0263-4.

37. Johnstone, D.N., Firth, F.C.N., Grey, C.P., Midgley, P.A., Cliffe, M.J., and Collins, S.M. (2020). Direct imaging of correlated defect nanodomains in a metal–organic framework. J. Am. Chem. Soc. *142*, 13081–13089. https://doi.org/10.1021/jacs.0c04468.

38. Ji, Z., Li, T., and Yaghi, O.M. (2020). Sequencing of metals in multivariate metal-organic frameworks. Science *369*, 674–680. https://doi.org/10.1126/science.aaz4304.

39. Goris, B., De Beenhouwer, J., De Backer, A., Zanaga, D., Batenburg, K.J., Sánchez-Iglesias, A., Liz-Marzán, L.M., Van Aert, S., Bals, S., Sijbers, J., et al. (2015). Measuring lattice strain in three dimensions through electron microscopy. Nano Lett. *15*, 6996–7001. https://doi.org/10.1021/acs.nanolett.5b03008.

40. Dou, J.-H., Arguilla, M.Q., Luo, Y., Li, J., Zhang, W., Sun, L., Mancuso, J.L., Yang, L., Chen, T., Parent, L.R., et al. (2021). Atomically precise single-crystal structures of electrically conducting 2D metal–organic frameworks. Nat. Mater. *20*, 222–228. https://doi.org/10.1038/s41563-020-00847-7.

41. Castano, I., Evans, A.M., dos Reis, R., Dravid, V.P., Gianneschi, N.C., and Dichtel, W.R. (2021). Mapping grains, boundaries, and defects in 2D covalent organic framework thin films. Chem. Mater. *33*, 1341–1352. https://doi.org/10.1021/acs.chemmater.0c04382.

42. Wei, J., Feng, B., Ishikawa, R., Yokoi, T., Matsunaga, K., Shibata, N., and Ikuhara, Y. (2021). Direct imaging of atomistic grain boundary migration. Nat. Mater. *20*, 951–955. https://doi.org/10.1038/s41563-020-00879-z.

43. Guzelturk, B., Winkler, T., Van de Goor, T.W.J., Smith, M.D., Bourelle, S.A., Feldmann, S., Trigo, M., Teitelbaum, S.W., Steinrück, H.-G., de la Pena, G.A., et al. (2021). Visualization of dynamic polaronic strain fields in hybrid lead halide perovskites. Nat. Mater. *20*, 618–623. https://doi.org/10.1038/s41563-020-00865-5.

44. Cavka, J.H., Jakobsen, S., Olsbye, U., Guillou, N., Lamberti, C., Bordiga, S., and Lillerud, K.P. (2008). A new zirconium inorganic building brick forming metal organic frameworks with exceptional stability. J. Am. Chem. Soc. *130*, 13850–13851. https://doi.org/10.1021/ja8057953.

45. Deria, P., Gómez-Gualdrón, D.A., Bury, W., Schaef, H.T., Wang, T.C., Thallapally, P.K., Sarjeant, A.A., Snurr, R.Q., Hupp, J.T., and Farha, O.K. (2015). Ultraporous, water stable, and breathing zirconium-based metal–organic frameworks with ftw topology. J. Am. Chem. Soc. *137*, 13183–13190. https://doi.org/10.1021/jacs.5b08860.

46. Garibay, S.J., and Cohen, S.M. (2010). Isoreticular synthesis and modification of frameworks with the UiO-66 topology. Chem. Commun. *46*, 7700–7702. https://doi.org/10.1039/C0CC02990D.

47. Kandiah, M., Usseglio, S., Svelle, S., Olsbye, U., Lillerud, K.P., and Tilset, M. (2010). Post-synthetic modification of the metal–organic framework compound UiO-66. J. Mater. Chem. *20*, 9848–9851. https://doi.org/10.1039/C0JM02416C.

48. Kaskel, S. (2016). The Chemistry of Metal-Organic Frameworks: Synthesis, Characterization, and Applications (John Wiley & Sons).

49. Bambalaza, S.E., Langmi, H.W., Mokaya, R., Musyoka, N.M., Ren, J., and Khotseng, L.E. (2018). Compaction of a zirconium metal–organic framework (UiO-66) for high density hydrogen storage applications. J. Mater. Chem. A *6*, 23569–23577. https://doi.org/10.1039/C8TA09227C.

50. Khabzina, Y., Dhainaut, J., Ahlhelm, M., Richter, H.-J., Reinsch, H., Stock, N., and Farrusseng, D. (2018). Synthesis and shaping scale-up study of functionalized UiO-66 MOF for ammonia air purification filters. Ind. Eng. Chem. Res. *57*, 8200–8208. https://doi.org/10.1021/acs.iecr.8b00808.

51. Valenzano, L., Civalleri, B., Chavan, S., Bordiga, S., Nilsen, M.H., Jakobsen, S., Lillerud, K.P., and Lamberti, C. (2011). Disclosing the complex structure of UiO-66 metal organic framework: a synergic combination of experiment and theory. Chem. Mater. *23*, 1700–1718. https://doi.org/10.1021/cm1022882.

52. DeCoste, J.B., Peterson, G.W., Jasuja, H., Glover, T.G., Huang, Y.-g., and Walton, K.S. (2013). Stability and degradation mechanisms of metal–organic frameworks containing the $Zr_6O_4(OH)_4$ secondary building unit. J. Mater. Chem. A *1*, 5642–5650. https://doi.org/10.1039/C3TA10662D.

53. Wu, H., Yildirim, T., and Zhou, W. (2013). Exceptional mechanical stability of highly porous zirconium metal–organic framework UiO-66 and its important implications. J. Phys. Chem. Lett. *4*, 925–930. https://doi.org/10.1021/jz4002345.

54. Peterson, G.W., DeCoste, J.B., Glover, T.G., Huang, Y., Jasuja, H., and Walton, K.S. (2013). Effects of pelletization pressure on the physical and chemical properties of the metal–organic frameworks $Cu_3(BTC)_2$ and UiO–66. Microporous Mesoporous Mater. *179*, 48–53. https://doi.org/10.1016/j.micromeso.2013.02.025.

55. Yot, P.G., Yang, K., Ragon, F., Dmitriev, V., Devic, T., Horcajada, P., Serre, C., and Maurin, G. (2016). Exploration of the mechanical behavior of metal organic frameworks UiO-66(Zr) and MIL-125(Ti) and their NH_2 functionalized versions. Dalton Trans. *45*, 4283–4288. https://doi.org/10.1039/C5DT03621F.

56. Rogge, S.M.J., Wieme, J., Vanduyfhuys, L., Vandenbrande, S., Maurin, G., Verstraelen, T., Waroquier, M., and Van Speybroeck, V. (2016). Thermodynamic insight in the high-pressure behavior of UiO-66: effect of linker defects and linker expansion. Chem. Mater. *28*, 5721–5732. https://doi.org/10.1021/acs.chemmater.6b01956.

57. Kandiah, M., Nilsen, M.H., Usseglio, S., Jakobsen, S., Olsbye, U., Tilset, M., Larabi, C., Quadrelli, E.A., Bonino, F., and Lillerud, K.P. (2010). Synthesis and stability of tagged UiO-66 Zr-MOFs. Chem. Mater. *22*, 6632–6640. https://doi.org/10.1021/cm102601v.

58. Leus, K., Bogaerts, T., De Decker, J., Depauw, H., Hendrickx, K., Vrielinck, H., Van Speybroeck, V., and Van Der Voort, P. (2016). Systematic study of the chemical and hydrothermal stability of selected "stable" metal organic frameworks. Microporous Mesoporous Mater. *226*, 110–116. https://doi.org/10.1016/j.micromeso.2015.11.055.

59. Shearer, G.C., Forselv, S., Chavan, S., Bordiga, S., Mathisen, K., Bjørgen, M., Svelle, S., and Lillerud, K.P. (2013). In situ infrared spectroscopic and gravimetric characterisation of the solvent removal and dehydroxylation of the metal organic frameworks UiO-66 and UiO-67. Top. Catal. *56*, 770–782. https://doi.org/10.1007/s11244-013-0027-0.

60. Wu, H., Chua, Y.S., Krungleviciute, V., Tyagi, M., Chen, P., Yildirim, T., and Zhou, W. (2013). Unusual and highly tunable missing-linker defects in zirconium metal–organic framework UiO-66 and their important effects on gas adsorption. J. Am. Chem. Soc. *135*, 10525–10532. https://doi.org/10.1021/ja404514r.

61. Shearer, G.C., Chavan, S., Ethiraj, J., Vitillo, J.G., Svelle, S., Olsbye, U., Lamberti, C., Bordiga, S., and Lillerud, K.P. (2014). Tuned to perfection: ironing out the defects in metal–organic framework UiO-66. Chem. Mater. *26*, 4068–4071. https://doi.org/10.1021/cm501859p.

62. Øien, S., Wragg, D., Reinsch, H., Svelle, S., Bordiga, S., Lamberti, C., and Lillerud, K.P. (2014). Detailed structure analysis of atomic positions and defects in zirconium metal–organic frameworks. Cryst. Growth Des. *14*, 5370–5372. https://doi.org/10.1021/cg501386j.

63. Trickett, C.A., Gagnon, K.J., Lee, S., Gándara, F., Bürgi, H.-B., and Yaghi, O.M. (2015). Definitive molecular level characterization of defects in UiO-66 crystals. Angew. Chem. Int. Ed. Engl. *54*, 11162–11167. https://doi.org/10.1002/anie.201505461.

64. Cliffe, M.J., Wan, W., Zou, X., Chater, P.A., Kleppe, A.K., Tucker, M.G., Wilhelm, H., Funnell, N.P., Coudert, F.-X., and Goodwin, A.L. (2014). Correlated defect nanoregions in a metal–organic framework. Nat. Commun. *5*, 4176. https://doi.org/10.1038/ncomms5176.

65. Dissegna, S., Vervoorts, P., Hobday, C.L., Düren, T., Daisenberger, D., Smith, A.J., Fischer, R.A., and Kieslich, G. (2018). Tuning the mechanical response of metal–organic frameworks by defect engineering. J. Am. Chem. Soc. *140*, 11581–11584. https://doi.org/10.1021/jacs.8b07098.

66. Rogge, S.M.J., Yot, P.G., Jacobsen, J., Muniz-Miranda, F., Vandenbrande, S., Gosch, J., Ortiz, V., Collings, I.E., Devautour-Vinot, S., Maurin, G., et al. (2020). Charting the metal-dependent high-pressure stability of bimetallic UiO-66 materials. ACS Mater. Lett. *2*, 438–445. https://doi.org/10.1021/acsmaterialslett.0c00042.

67. Rogge, S.M.J., Waroquier, M., and Van Speybroeck, V. (2019). Unraveling the thermodynamic criteria for size-dependent spontaneous phase separation in soft porous crystals. Nat. Commun. *10*, 4842. https://doi.org/10.1038/s41467-019-12754-w.

68. Braess, D. (1968). Über ein Paradoxon aus der Verkehrsplanung. Unternehmensforschung Oper. Res. *12*, 258–268. https://doi.org/10.1007/BF01918335.

69. Pala, M.G., Baltazar, S., Liu, P., Sellier, H., Hackens, B., Martins, F., Bayot, V., Wallart, X., Desplanque, L., and Huant, S. (2012). Transport inefficiency in branched-out mesoscopic networks: an analog of the Braess paradox. Phys. Rev. Lett. *108*, 076802. https://doi.org/10.1103/PhysRevLett.108.076802.

70. Nagurney, L.S., and Nagurney, A. (2016). Physical proof of the occurrence of the Braess paradox in electrical circuits. Europhys. Lett. *115*, 28004. https://doi.org/10.1209/0295-5075/115/28004.

71. Mason, J.A., Oktawiec, J., Taylor, M.K., Hudson, M.R., Rodriguez, J., Bachman, J.E., Gonzalez, M.I., Cervellino, A., Guagliardi, A., Brown, C.M., et al. (2015). Methane storage in flexible metal–organic frameworks with intrinsic thermal management. Nature *527*, 357–361. https://doi.org/10.1038/nature15732.

72. Dybtsev, D.N., Chun, H., and Kim, K. (2004). Rigid and flexible: a highly porous metal-organic framework with unusual guest-dependent dynamic behavior. Angew. Chem. Int. Ed. Engl. *43*, 5033–5036. https://doi.org/10.1002/anie.200460712.

73. Nanthamathee, C., Ling, S., Slater, B., and Attfield, M.P. (2015). Contradistinct thermoresponsive behavior of isostructural MIL-53 type metal–organic frameworks by modifying the framework inorganic anion. Chem. Mater. *27*, 85–95. https://doi.org/10.1021/cm503311x.

74. Rogge, S.M.J., Vanduyfhuys, L., Ghysels, A., Waroquier, M., Verstraelen, T., Maurin, G., and Van Speybroeck, V. (2015). A comparison of barostats for the mechanical characterization of metal–organic frameworks. J. Chem. Theory Comput. *11*, 5583–5597. https://doi.org/10.1021/acs.jctc.5b00748.

75. Rogge, S.M.J., Waroquier, M., and Van Speybroeck, V. (2018). Reliably modeling the mechanical stability of rigid and flexible metal-organic frameworks. Acc. Chem. Res. *51*, 138–148. https://doi.org/10.1021/acs.accounts.7b00404.

76. Vanduyfhuys, L., Vandenbrande, S., Verstraelen, T., Schmid, R., Waroquier, M., and Van Speybroeck, V. (2015). QuickFF: a program for a quick and easy derivation of force fields for metal–organic frameworks from ab initio input. J. Comput. Chem. *36*, 1015–1027. https://doi.org/10.1002/jcc.23877.

77. Vanduyfhuys, L., Vandenbrande, S., Wieme, J., Waroquier, M., Verstraelen, T., and Van Speybroeck, V. (2018). Extension of the QuickFF force field protocol for an improved accuracy of structural, vibrational, mechanical and thermal properties of metal–organic frameworks. J. Comput. Chem. *39*, 999–1011. https://doi.org/10.1002/jcc.25173.

78. Chen, J., and Martínez, T.J. (2007). QTPIE: charge transfer with polarization current equalization. A fluctuating charge model with correct asymptotics. Chem. Phys. Lett. *438*, 315–320. https://doi.org/10.1016/j.cplett.2007.02.065.

79. Halgren, T.A. (1996). Merck molecular force field. II. MMFF94 van der Waals and electrostatic parameters for intermolecular interactions. J. Comput. Chem. *17*, 520–552. https://doi.org/10.1002/(SICI)1096-987X(199604)17:5/6<520::AID-JCC2>3.0.CO;2-W.

80. Lii, J.H., and Allinger, N.L. (1989). Molecular mechanics. The MM3 force field for hydrocarbons. 3. The van der Waals' potentials and crystal data for aliphatic and aromatic hydrocarbons. J. Am. Chem. Soc. *111*, 8576–8582. https://doi.org/10.1021/ja00205a003.

81. Verstraelen, T., Vanduyfhuys, L., Vandenbrande, S., and Rogge, S.M.J. (2023). Yaff, yet another force field. http://molmod.ugent.be/software/.

82. Plimpton, S. (1995). Fast parallel algorithms for short-range molecular dynamics. J. Comput. Phys. *117*, 1–19. https://doi.org/10.1006/jcph.1995.1039.

83. Nosé, S. (1984). A molecular dynamics method for simulations in the canonical ensemble. Mol. Phys. *52*, 255–268. https://doi.org/10.1080/00268978400101201.

84. Nosé, S. (1984). A unified formulation of the constant temperature molecular dynamics methods. J. Chem. Phys. *81*, 511–519. https://doi.org/10.1063/1.447334.

85. Hoover, W.G. (1985). Canonical dynamics: equilibrium phase-space distributions. Phys. Rev. A *31*, 1695–1697. https://doi.org/10.1103/PhysRevA.31.1695.

86. Martyna, G.J., Klein, M.L., and Tuckerman, M. (1992). Nosé-Hoover chains: the canonical ensemble via continuous dynamics. J. Chem. Phys. *97*, 2635–2643. https://doi.org/10.1063/1.463940.

87. Martyna, G.J., Tobias, D.J., and Klein, M.L. (1994). Constant pressure molecular dynamics algorithms. J. Chem. Phys. *101*, 4177–4189. https://doi.org/10.1063/1.467468.

88. Martyna, G.J., Tuckerman, M.E., Tobias, D.J., and Klein, M.L. (1996). Explicit reversible integrators for extended systems dynamics. Mol. Phys. *87*, 1117–1157. https://doi.org/10.1080/00268979600100761.

89. Ewald, P.P. (1921). Die Berechnung optischer und elektrostatischer Gitterpotentiale. Ann. Phys. *369*, 253–287. https://doi.org/10.1002/andp.19213690304.

90. Dubbeldam, D., Calero, S., and Vlugt, T.J.H. (2018). iRASPA: GPU-accelerated visualization software for materials scientists. Mol. Simul. *44*, 653–676. https://doi.org/10.1080/08927022.2018.1426855.

91. Humphrey, W., Dalke, A., and Schulten, K. (1996). VMD: visual molecular dynamics. J. Mol. Graph. *14*, 33–38. https://doi.org/10.1016/0263-7855(96)00018-5.

92. Willems, T.F., Rycroft, C.H., Kazi, M., Meza, J.C., and Haranczyk, M. (2012). Algorithms and tools for high-throughput geometry-based analysis of crystalline porous materials. Microporous Mesoporous Mater. *149*, 134–141. https://doi.org/10.1016/j.micromeso.2011.08.020.